*Geophys. J. Int.* (2005) **163,** 56–78 doi: 10.1111/j.1365-246X.2005.02738.x

# Temporal and spatial cyclicity of accretion at slow-spreading ridges—evidence from the Reykjanes Ridge

Christine Peirce,[1] Alex Gardiner[2] and Martin Sinha[3]

[1]*Department of Earth Sciences, University of Durham, Science Laboratories, South Road, Durham,* DH1 3LE, *UK. E-mail: Christine.Peirce@durham.ac.uk*
[2]*British Oceanographic Data Centre, Bidston Observatory, Bidston Hill, Prenton, Merseyside,* CH43 7RA, *UK*
[3]*School of Ocean and Earth Science, Southampton Oceanography Centre, University of Southampton, European Way, Southampton,* SO14 3ZH, *UK*

Accepted 2005 July 4. Received 2005 June 30; in original form 2004 August 20

## SUMMARY

A unifying model of oceanic crustal development at slow spreading rates is presented in which accretion follows a cyclic pattern of magmatic construction and tectonic destruction, controlled by along-axis variation in melt supply and coupled to along-axis variation in spreading rate and across-axis asymmetry in spreading.

This study focuses on the Reykjanes Ridge, Mid-Atlantic Ridge south of Iceland, which is divided along its entire length into numerous axial volcanic ridges (AVR). Five adjacent AVRs have been analysed, located between 57°30′N and 58°30′N and south of any strong Iceland hotspot influence. The seabed morphology of each AVR is investigated using sidescan sonar data to determine relative age and eruptive history. Along-axis gravity profiles for each AVR are modelled relative to a seismically derived crustal reference model, to reveal the underlying crustal thickness and density structure. Correlating these models with seabed features, crustal structure, ridge segment morphology and relative ages, a model of cyclic ridge segmentation is developed in which accretion results in adjacent AVRs with a range of crustal features which, when viewed collectively, reveal that second-order segments on the Reykjanes Ridge have an along-axis length of ∼70 km and comprise several adjacent AVRs which, in turn, reflect the pattern of third-order segmentation. Tectono-magmatic accretion is shown to operate on the scale of individual AVRs, as well as on the scale of the second-order segment as a whole.

**Key words:** crustal accretion, crustal structure, gravity anomalies, mid-ocean ridges, oceanic crust, residual mantle Bouguer anomaly.



## 1 INTRODUCTION

The wealth of swath bathymetry data acquired at mid-ocean ridges shows that they are segmented on a variety of scales. Coincident geophysical and geochemical surveys have shown that this segmentation is reflected along axis in crustal structure and composition as well as thickness. Observations suggest that ridge segmentation is controlled by along-axis variation in melt supply and that the variation in the rate of this supply plays a significant role in the mode by which new oceanic crust accretes.

The episodicity of crustal accretion at slow spreading rates has been highlighted by a comprehensive multidisciplinary study of an axial volcanic ridge segment (AVR) of the slow-spreading Mid-Atlantic Ridge (MAR). The RAMESSES (*R*eykjanes *A*xial *M*elt *E*xperiment: *S*tructural *S*ynthesis from *E*lectromagnetics and *S*eismics—Sinha *et al.* 1997, 1998; MacGregor *et al.* 1998; Navin *et al.* 1998; Heinson *et al.* 2000; Peirce & Navin 2002; Topping 2002; Gardiner 2003) experiments provided evidence from the combined interpretation of wide-angle seismic, normal incidence seismic, gravity, controlled source electromagnetic (CSEM) and magnetotelluric (MT) data (see Fig. 1) for the existence of a magma chamber beneath an AVR at 57°45′N on the Reykjanes Ridge, which contains 20–40 per cent partial melt (Heinson *et al.* 2000; MacGregor *et al.* 1998), with sufficient melt volume to support ∼20 000 yr of crustal accretion, and which would cool to subsolidus temperatures within ∼1500 yr (MacGregor *et al.* 1998). The contrast between cooling rate and accretion duration, therefore, implies an accretionary process which has magmatic and amagmatic phases.

Beneath the RAMESSES AVR the upper mantle down to a depth of ∼50 km below sea level (bsl) is effectively melt free, while between ∼50 and 100 km bsl partial melt is present (Heinson *et al.* 2000), which has implications for the mode of delivery of melt from the mantle to the crust (Sinha *et al.* 1998). Heinson *et al.* (2000) suggest that the 50–100 km zone is where adiabatic decompression melting forms a layer of partial melt, with its episodic transport to the crust occurring either through conduits or through pervasive flow. Alternatively, the region between the base of the crust and ∼50 km bsl could itself also be a source of melt, but which has recently been depleted by rapid transport to the crust. In both cases, the absence of a clear conduit or connection between the

 

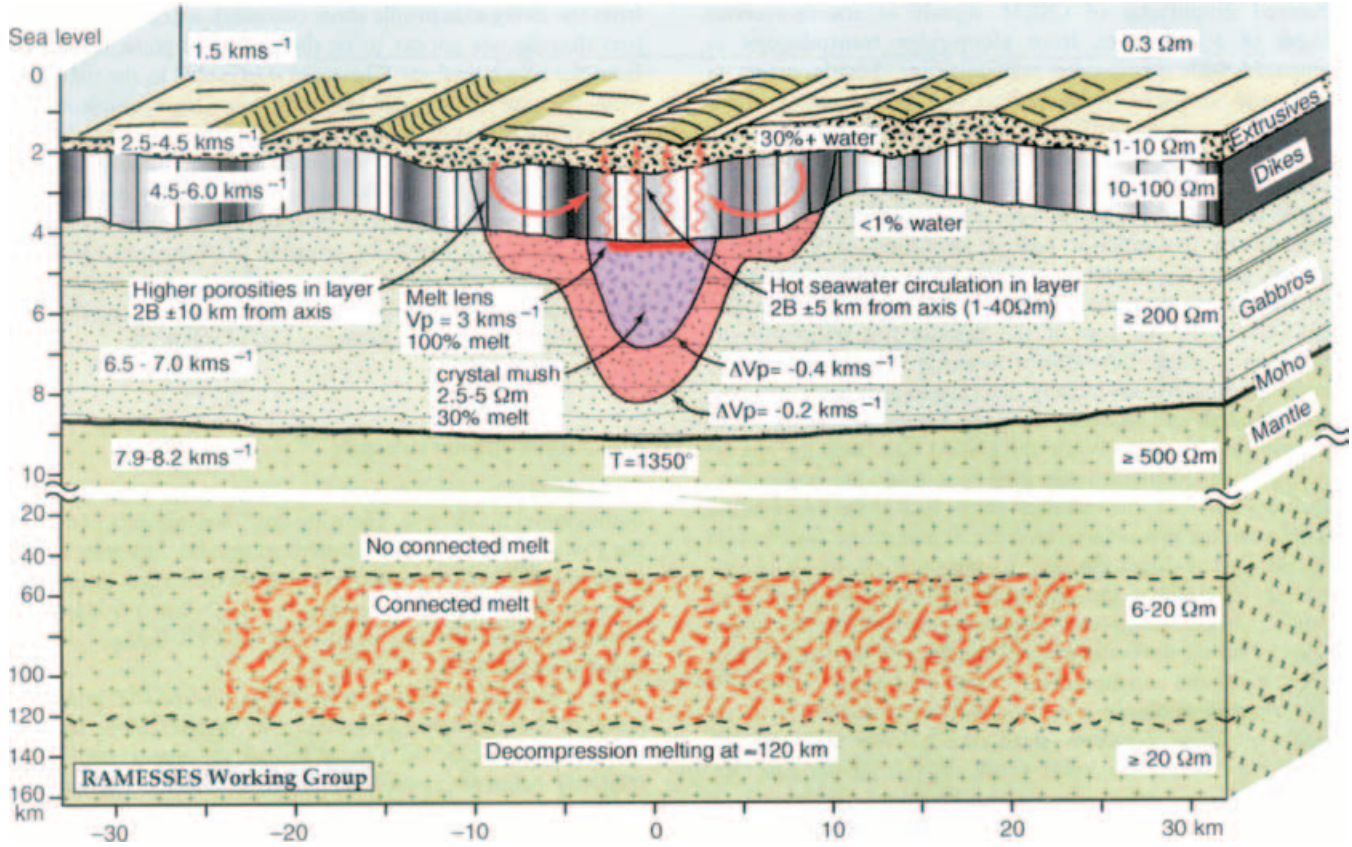


**Figure 1.** Cross-sectional model of the 57°45′N AVR based on a synthesis of the modelling and interpretation of RAMESSES data sets. The analyses of seismic, gravity, electromagnetic and magnetotelluric data suggest that a magma chamber underlies this AVR and that a zone of partial melt extends from ~50 to 100 km depth in the upper mantle. Note that a break in scale occurs at a depth of 10 km below sea level. After Sinha *et al.* (1998).

melt source and accumulation zones suggests that it is the supply of melt from the mantle to crust that is episodic and, in turn, it is that episodicity that leads to periods of magmatic and amagmatic crustal accretion.

Despite extensive geophysical surveying of the global mid-ocean ridge system prior to the RAMESSES experiment, the latter was the first unequivocal observation of an active magmatic system beneath ridges classified as spreading at slow rates. Contrary to the widely accepted view at that time that crustal melt bodies, even of small dimensions, could not be maintained at slow spreading rates due to an inadequate heat flux, the results of the RAMESSES project showed that they can and do exist. Thus the apparent contradiction between the requirement for crustal melt bodies to explain structural and petrological observations and the majority of geophysical observations (until RAMESES) that suggest that they do not exist, is best explained if melt-filled magma chambers are transient features, related to the episodic influx of melt from the mantle; the consequence of which is a cyclic pattern of accretion. On this basis geophysical observations of crustal melt bodies will be dependent on identifying a segment that is in the appropriate stage of its life cycle, with observation essentially being dependent on being in the right place at the right time.

The magma chamber model of the RAMESSES Working Group (Sinha *et al.* 1998) is similar, in terms of its layer thicknesses, geometries and properties, to magma chambers imaged at faster-spreading ridges using similar surveying methods. This suggests that processes of crustal accretion are similar at all spreading rates but, significantly, it is the temporal variability in melt transport from the upper mantle to the crust which underpins the differences between the crustal structure and seabed morphology.

Parson *et al.* (1993), in a separate sidescan sonar study at the Reykjanes Ridge, showed that during periods of magmatic quiescence AVRs undergo extensive dismemberment by tectonic forces, while magmatic periods are evidenced by volcanic eruption. The cyclicity of crustal accretion is, therefore, imprinted into the seafloor morphology. However, the temporal dimension to this cyclic accretion is poorly understood, with recent studies (e.g. Stewart *et al.* 2002) suggesting that temporal variability in melt transport is a significant process even at fast-spreading ridges. Such so-called tectonomagmatic cycles may, therefore, reflect a fundamental process in crustal accretion that operates at all spreading rates.

The existing extensive, diverse and comprehensive data sets that exist at the Reykjanes Ridge make it an ideal location to study the apparent relationship between the seafloor expression of tectonomagmatic cycles, the underlying crustal structure, the melt supply and accumulation process, the timescales of cycles and periodicity of melt influx, and their relationship to along-axis segmentation.

## 2 SETTING

The Reykjanes Ridge is a 900 km section of the slow-spreading MAR running from the Bight fracture zone at 57°N to the Reykjanes Peninsula on Iceland at 63°N (Fig. 2). Interaction with the Iceland hotspot results in an axial morphology which changes in style from median valley in the south to axial rise in the north, accompanied by a general shallowing of the seafloor towards Iceland.

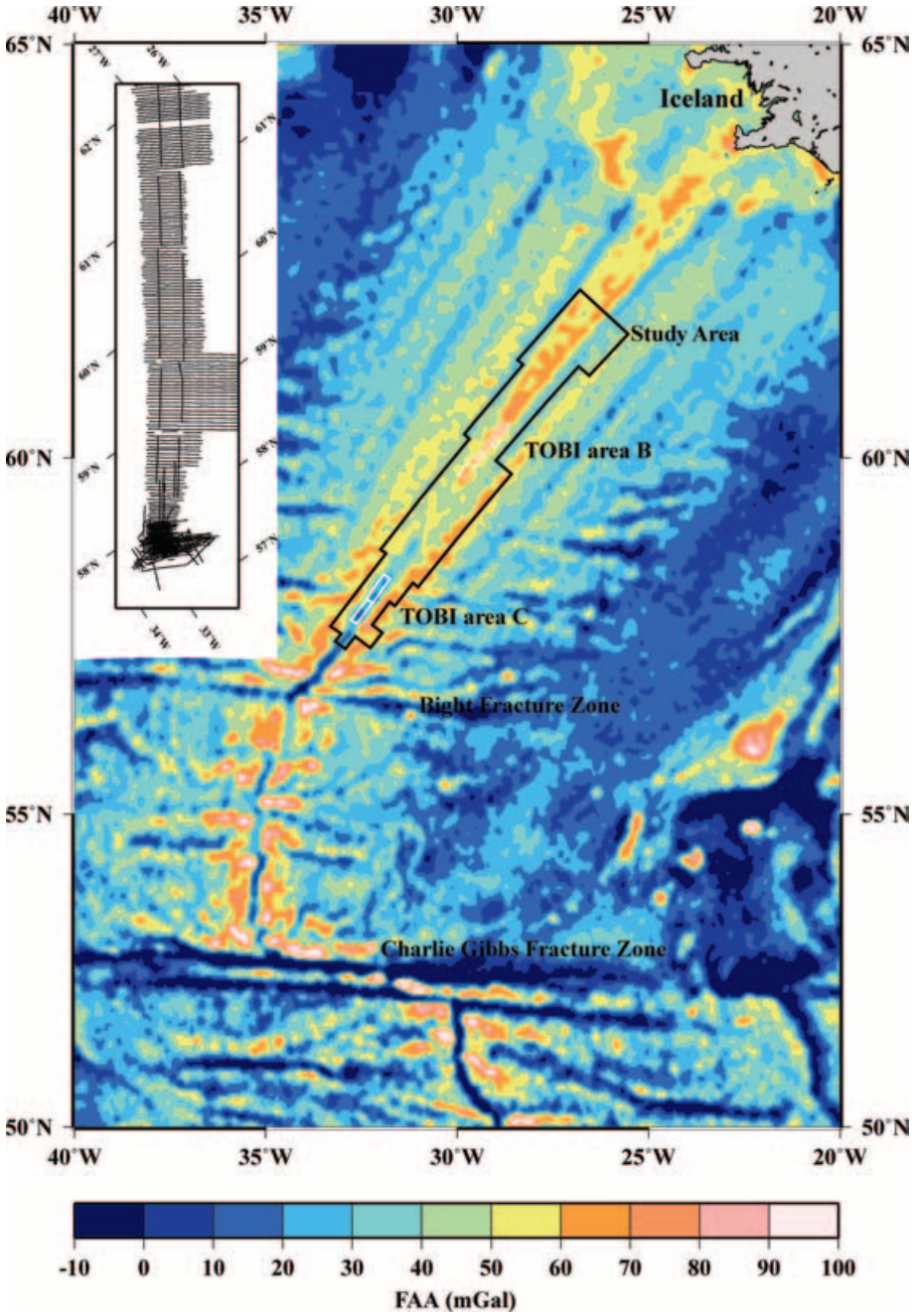


**Figure 2.** Free-air gravity anomaly of the North Atlantic (Sandwell & Smith 1997) shaded to highlight the location of the Reykjanes Ridge and showing the change in ridge orientation at the Bight fracture zone. Also clearly visible are the southerly trending V-shaped ridges thought to be the result of hotspot pulsing (Ito 2001). The location of the study area is outlined. Note that the change from median valley to the axial high topography associated with the Iceland hotspot can clearly be seen at ∼59°N. Inset shows the location of the ship tracks along which the gravity, magnetic and bathymetry data modelled in this paper were acquired. The white outlines show the locations of the TOBI sidescan sonar data acquired during EW9008/90.

Ito (2001) proposes that magmatic pulsing of the hotspot leads to thermal perturbations that propagate radially away from its centre. Interaction with the ridge axis results in periods of accretion during which melt supply is enhanced and thicker crust generated within the region of influence. Southwards propagation of these pulses along the ridge axis is thought to give rise to the V-shaped ridges clearly visible in the gravity field (see Fig. 2— Vogt 1971).

The ridge follows a trend of 036° which is oblique to the spreading direction of 096° (DeMets *et al.* 1990), and results in two trends in seabed features—one ridge-parallel and one perpendicular to the spreading direction. AVRs are oriented orthogonal to the spreading direction and are separated by right-stepping en-echelon offsets. Faulting is predominantly perpendicular to the spreading direction within the neovolcanic, axial region but rotates to a ridge-parallel trend off-axis.

Parson *et al.* (1993) further developed their seabed observations into a model of crustal accretion, which suggests that each AVR has its own life span comprising a period of magmatic accretion followed by a period of amagmatic extension. During the *magmatic phase* vigorous volcanism leads to the formation and rapid

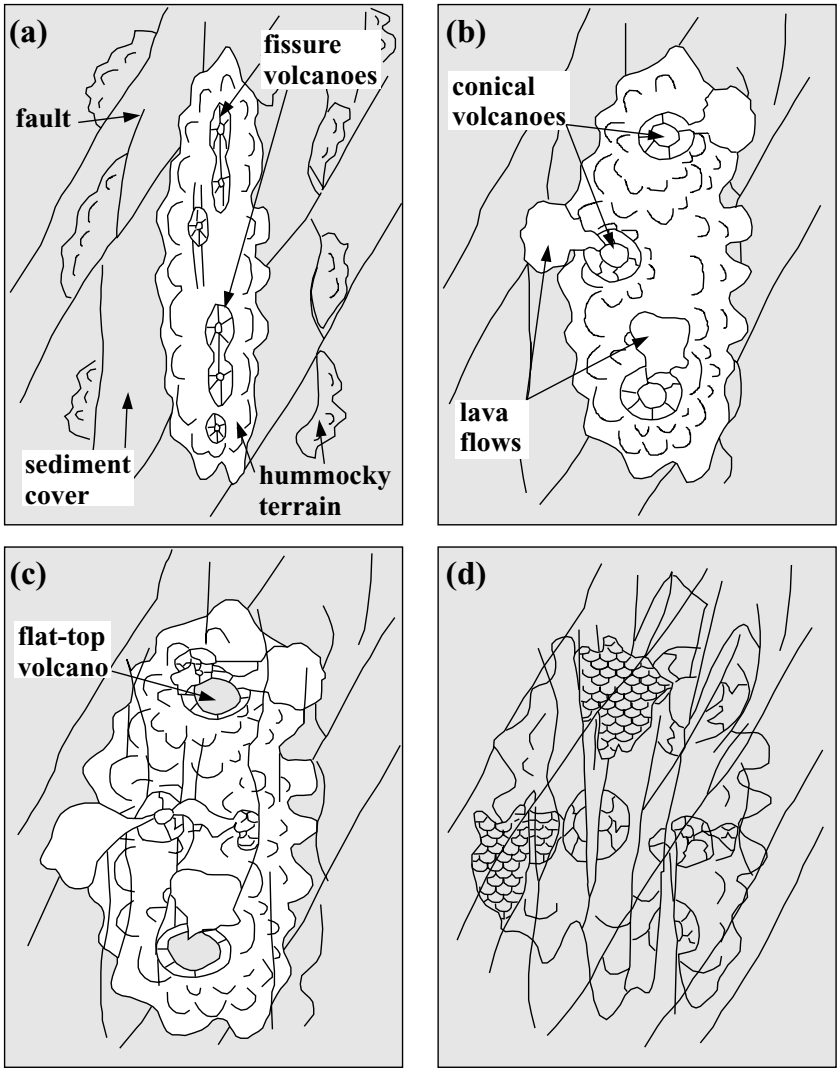


**Figure 3.** Tectono-magmatic accretion after Parson *et al.* (1993), showing an AVR at various stages in its life cycle. The *magmatic* phase comprises the *young* (a) and *adolescent* (b) stages, while the *tectonic* phase includes the *mature* (c) and *old* (d) stages. Note that as the life cycle progresses there is a change from fissure to conical to flat-topped (shield) volcanoes, reflecting the mode of magma delivery to the seafloor. As AVRs age through their life cycle the dominant direction of faulting changes from spreading orthogonal to ridge-parallel until, eventually, each AVR is completely dismembered.

growth of a linear axial volcano (the AVR), which typically extends up to ∼35 km along-axis (the *young* stage) (Fig. 3), with AVRs only reaching full maturity as the rate of magmatic activity starts to decline (the *adolescent* stage). With on-going seafloor spreading during the later stages of the magmatic phase and throughout the post-magmatic or *tectonic phase*, AVRs become dissected by many spreading-orthogonal faults (the *mature* stage). Eventually, the volcanic terrain of the magmatic phase becomes overprinted by younger tectonic features and, ultimately, extinct AVRs become completely dismembered by faulting (the *old* stage). Ultimately a new magmatic phase is initiated, leading at first to isolated fresh lava flows that overprint the tectonized seafloor, and then to the establishment and growth to maturity of a new AVR—the duration of a cycle being ∼0.5 Myr (Searle *et al.* 1998). Under Parson *et al*.'s (1993) tectono-magmatic model, a cycle is defined by the *young* and *adolescent* stages of the *magmatic* phase and the *mature* and *old* stages of the *tectonic* phase. As crustal structure is intimately related to melt supply, AVRs in their magmatic phase should, therefore, differ from those undergoing tectonic extension, or from ones at the very beginning of their life cycle. Thus, Parson *et al*.'s (1993) approach provides a set of starting assumptions by which adjacent AVRs may be relatively aged.

## 3 THE DATA SET

To investigate inter-AVR relationships in the context of the hypothesis of tectono-magmatic life cycles of accretion requires: (1) a set of adjacent AVRs located in a region broadly unaffected by hotspot influence (i.e. south of 59°N); (2) co-incident gravity, magnetic and bathymetry data; and most importantly, (3) sidescan sonar data coverage with which to characterize the seabed morphology.

The results presented in this paper are based upon the analysis and interpretation of geophysical data acquired during a number of research cruises undertaken between 1990 and 1998 (syntax: cruise number/year—*RRS Charles Darwin* CD81/93, *R/V Maurice Ewing* EW9008/90, *RRS Charles Darwin* CD87/94 and *RRS Discovery* D235c/98—Parson 1993; Searle *et al.* 1994b; Sinha *et al.* 1994; Peirce & Sinha 1998, respectively). The bathymetry data from the first three of these forms the basis of the compilation by Keeton

*et al.* (1997), while the corresponding magnetic data form the basis of the compilation of Lee & Searle (2000).

Bathymetry data is used to create an accurate representation of the seabed at sub-AVR scale, while sidescan sonar images of the ridge axis are used to characterize and identify the morphology of each AVR and thus identify its life cycle stage and relative age. Gravity modelling, in both 2-D and 3-D, is used to investigate along-axis crustal structure variations, while magnetic data are inverted in 3-D to obtain magnetization intensity variations and provide an indication of the relative age of the extrusives. In addition, for each AVR studied, the rate and symmetry of spreading is also investigated. The various stages in data compilation and processing are very briefly outlined below and fuller details can be found in the cited literature.

It must be noted that the results of modelling of these data sets is only significant to the scale of their individual resolutions. Consequently, the conclusions drawn in this paper relate mostly to the geophysical perception of the oceanic crust and the larger-scale processes operating therein.

### 3.1 Bathymetry data

Shipboard swath bathymetry data coverage of the Reykjanes Ridge encompasses the ridge axis and up to 50 km (5 Ma) off-axis from 57°30′N to 62°N (see Fig. 2 inset for ship track coverage). For this study, coverage was extended to 100 km (10 Ma) off-axis and holes in the swath coverage patched by incorporating data extracted from Sandwell & Smith's (1997) satellite data set. These data were merged, smoothed and gridded—see Keeton *et al.* (1997) for details. The resulting ridge bathymetry data set is shown in Fig. 4(a).

South of 59°N, the median valley topography characteristic of slow-spreading ridges predominates, while north of 59°N an axial rise more characteristic of intermediate- and faster-spreading ridges exists. As this change in morphology is attributed to the influence of the nearby Iceland hotspot, 59°N is regarded as marking the southerly limit of direct hotspot–ridge interaction (Sinha *et al.* 1997, 1998; Peirce & Navin 2002). This assumption will be tested in Section 5.1.

### 3.2 Gravity data

The ship-based gravity data set comprises 337 profiles spaced, on average, 3.5–5 km along-axis and crossover analysis was performed on each individual cruise data set to minimize cruise specific errors. Profiles from each contributing data set were then compared to ensure a consistent datum level between cruises prior to merging. A crossover analysis of the merged data was then performed prior to gridding to minimize the root-mean-square (rms) error for the entire data set to ±1 mGal. The free-air anomaly (FAA) shown in Fig. 4(b) was obtained by gridding with node parameters and footprint area matching the bathymetry data, and with any off-axis gaps patched in the same manner.

The FAA pattern mirrors the ridge topography (Fig. 4a). As the seabed shoals heading northwards the axial anomaly increases from ∼ +10 mGal at 57°25′N to ∼ +65 mGal at 62°N. FAA values of less than ∼ +40 mGal occur over the median valley with local minima of ∼ +20 mGal associated with inter-AVR basins, whereas the axial rise morphology of the ridge is characterized by a FAA mean value of ∼ +50 mGal with local maxima of ∼ +70 mGal associated with larger AVRs. Prominent larger-scale features of the FAA are the V-shaped ridges (Vogt 1971; Ito 2001). These ridges are also evident in the bathymetry data set but to a far lesser degree (Fig. 4a), most probably due to sediment cover (Jones *et al.* 2002).

The observed long-wavelength increase in FAA heading northwards suggests that the elevated seabed topography associated with the Iceland hotspot is not in complete isostatic equilibrium but instead may be partly supported dynamically by processes associated with the plume in the mantle. This observation will be considered further in Section 5.

### 3.3 Magnetic data

The magnetic anomaly compilation of Lee & Searle (2000) was supplemented with data acquired during D235c/98 to complete coverage along-axis from 57°30′N to 62°30′N and up to 100 km off-axis. The combined magnetic anomaly is shown in Fig. 4(c).

### 3.4 Seabed image data

Two areas of sidescan sonar data were acquired during EW9008/90 (see Fig. 2 for location) using the Towed Ocean-Bottom Instrument—TOBI (Rouse 1991). One, TOBI area B, is located at the northern end of the ridge and one, TOBI area C, to the south. Only AVRs in TOBI area C, extending from 31°46′W to 32°47′W and 57°45′N to 58°27′N (see Fig. 2) and south of the assumed maximum extent of hotspot influence, were considered in terms of the characteristic features of axial lava flows, the degree and orientation of faulting and individual AVR length. The interrelationship between adjacent AVRs was also considered. The average seafloor depth in this region is ∼1950 m and AVRs shallow by up to ∼500 m above the surrounding terrain. Median valley faults, 10–12 km apart with seabed offsets of ∼500 m, are prominent features that extend up to 30 km in length in a flip-flop fashion, that is, alternating from one side of the ridge axis to the other, giving rise to asymmetric axial graben in cross-section. An example collation of TOBIgrams from the axial region between 57°45′N and 58°27′N is shown in Fig. 5.

## 4 TOBI DATA INTERPRETATION

AVRs identified in the TOBI data were initially interpreted in terms of their relative age by adopting the morphology vs. age definition of Parson *et al.* (1993), which is based upon the following assumptions. Thin AVRs associated with fissure-type volcanism are classified as *young*, and broader AVRs with conical seamounts are interpreted to be slightly older and placed at the *adolescent* stage of the cycle. *Mature* AVRs have flat-topped seamounts and are generally periclinal in shape with a few AVR-parallel faults, whereas *old* AVRs are covered by a thin layer of sediment and are dissected by ridge-parallel faults. However, for this study this relative ageing scheme was extended to allow a finer scale of relative age subdivision whereby AVRs that fall into the same age group (i.e. *young*, *adolescent*, *mature* or *old*) are separated further by taking into account the abundance of sediment cover and the extent of faulting.

The RAMESSES AVR lies at the southernmost extremity of TOBI area C. It was chosen to provide a unique geophysical reference, since its crust and upper mantle structure are well constrained by the RAMESSES studies, allowing seabed features to be directly related to underlying magmatic structures both in the crust and mantle (Sinha *et al.* 1997, 1998; MacGregor *et al.* 1998; Navin *et al.* 1998; Heinson *et al.* 2000).

The AVR numbering scheme of Keeton *et al.* (1997) was adopted for this study. This defines the RAMESSES AVR, at 57°45′N, as AVR 1 with AVR numbers increasing incrementally northwards from this point. Although the characteristics of all mapped AVRs

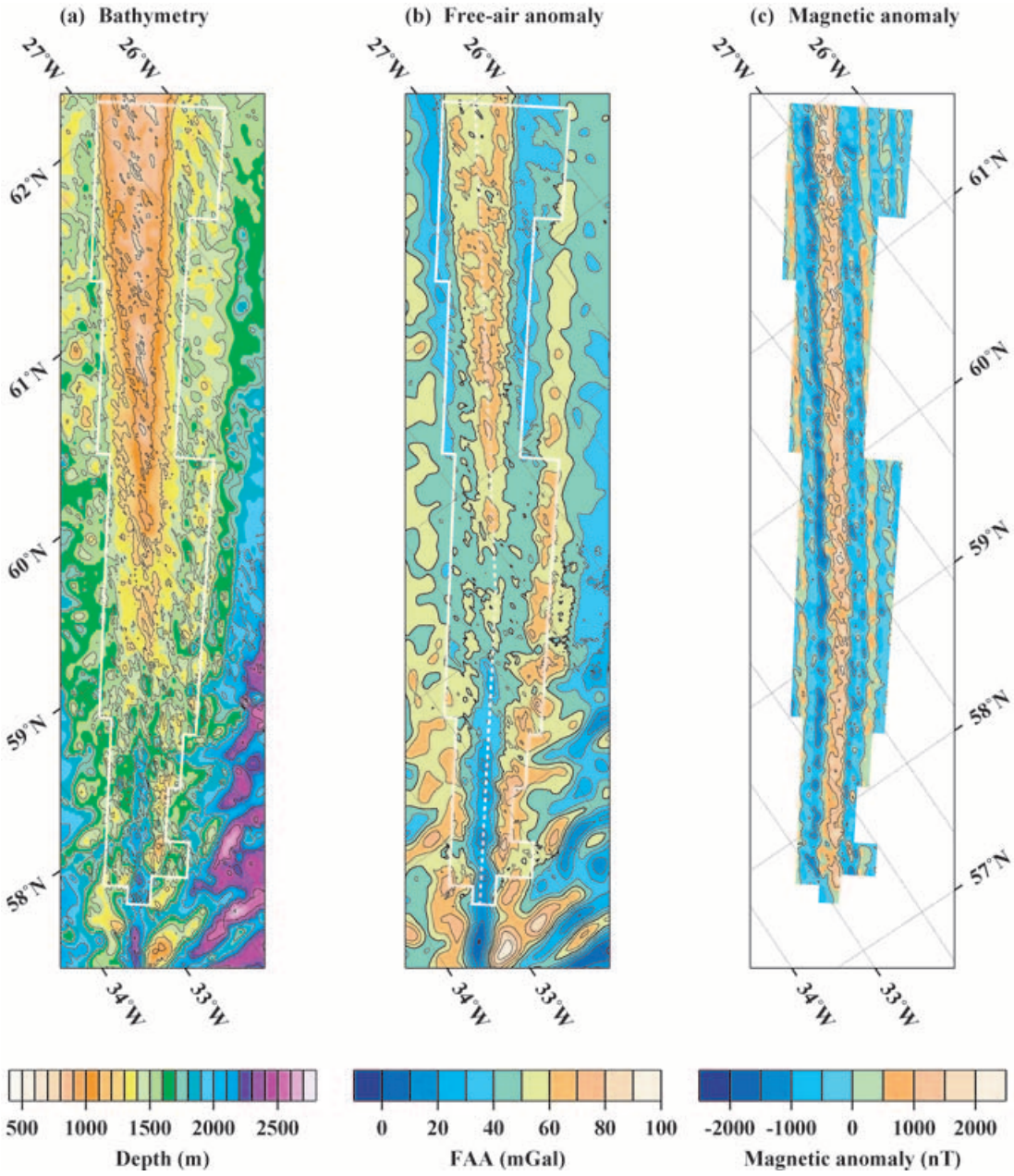


**Figure 4.** Reykjanes Ridge geophysical data set. (a) Bathymetry data compilation. The axial ridge morphology changes from an axial high north of ~59°N to a median valley to the south. Bathymetric contours are plotted at 250 m intervals. (b) Free-air gravity anomaly compilation. The gravity anomalies mirror the seafloor topography with the transition from median valley to axial rise morphology particularly clear. Contours are plotted at 10 mGal intervals. (c) Magnetic anomaly compilation showing only the region covered by ship tracks. Contour interval is 1000 nT. The dashed line on (b) shows the location of the along-axis profile modelled in Fig. 6. The outline box in all cases highlights the combined area surveyed by the cruises.

along the entire ridge axis were investigated, for the purposes of this paper AVRs 1, 2, 4, 6 and 7 were chosen as examples to show morphological type, age progression, inter-AVR relationships, spreading geometry and corresponding whole crustal structure within the region of focus.

To understand and map the variation in seabed morphology four types of terrain were defined based on the sidescan sonar textures (*cf.* key on Fig. 5). These are: *sediment*—to reflect areas of sediment cover; *hummocky*—to reflect areas of larger pillow mounds or accumulations; *hummocky (fine)*—to reflect areas of smaller pillow mounds or accumulations and *smooth*—to reflect sheet-like flows.

### 4.1 AVR 1 (RAMESSES)

This ~30 km long AVR centred on 57°45′N consists of a hummocky ridge with cratered conical and flat-topped volcanoes superimposed. Bright backscatter around the edges of this AVR indicates the presence of recent lava flows (Fig. 5). There is no clear evidence of faulting on the AVR itself but large AVR-parallel faults occur to its east, with similar smaller offset faults cutting off-axis hummocky terrain to the west. Little to no sediment cover is observed on-axis. Combined interpretation of the RAMESSES results (Sinha *et al.* 1998) suggests that this AVR is at the *young* to *adolescent* stage. However, its low magnetization, combined with a number of

local highs over small topographic features, led Lee & Searle (2000) to suggest that this AVR may be older and undergoing late-stage volcanism. The long length of this AVR, its broad convex shape, and the presence of cratered conical and flat-topped volcanoes, suggest a more mature phase of the cycle and that the recent extrusive volcanism is overprinting faulting on the AVR giving it a younger appearance.

### 4.2 AVR 2

This relatively short AVR (∼10 km) near 57°55′N is composed mainly of pillow lava terrain with some flows that are sediment covered in places (Fig. 5). A large, faulted, flat-topped volcano can be seen at its southern end and an unfaulted, but heavily sedimented, flat-topped volcano at the northern end. Two short AVR-trending hummocky ridges lie at the northern end of this AVR, while numerous small, ridge-trending faults overprint it entirely. The patchy sediment cover, extensive small-offset faulting and flat-topped volcanoes suggest that this AVR is at the very end *adolescent* to earliest *mature* phase of the cycle.

### 4.3 AVR 4

The ∼35-km-long hummocky edifice at 58°05′N contains one sediment covered, flat-topped volcano located towards the southeast (Fig. 5). Faulting is more extensive than for AVR 2 and mainly follows the ridge trend. Patchy sediment cover is visible on the edges of the volcanic terrain. This AVR is the longest, and appears to be the oldest, of the five AVRs studied and is probably at the early stages of the *mature* part of the cycle.

### 4.4 AVR 6

At this 58°15′N-centred ∼11-km-long AVR (Fig. 5) a degree of bright backscatter is observed around the edges, possibly indicating the presence of fresh lava flows. The volcanic terrain is mainly hummocky in appearance with no point volcanoes observed. Ridge-parallel faulting is only observed off-axis to the west. This AVR is younger in appearance than AVR 4, and is, most likely, at the *young* to *adolescent* stage of the cycle.

### 4.5 AVR 7

Fresh lava flows are observed around the edges of this ∼20 km long hummocky AVR located at 58°24′N (Fig. 5). There is no clear evidence for on-axis faulting, although faulting is prevalent off-axis to the north. Patchy sediment cover on its edges suggests that this AVR is younger than AVR 4 but slightly older than AVR 6, probably at the *adolescent* part of its cycle.

### 4.6 Summary of TOBI area C

TOBI area C contains AVRs that are mainly *adolescent* to *mature* in age. AVRs are well defined with a number of conical and flat-topped volcanoes observed. Faulting is ubiquitous off-axis but less prevalent on-axis, where it is generally parallel to the AVR spreading-orthogonal trend.

AVR morphology shows variation in the relative age and reveals a correlation between AVR age and length—shorter AVRs appearing younger than longer AVRs. An along-axis spatial wavelength of ∼70 km is observed in the relative age pattern, with those younger and shorter being found to the north and south of the oldest and longest AVR (AVR 4). This pattern of AVR lengths and characteristics is also observed in the bathymetry data to repeat along the ridge axis to the north, suggesting that AVRs are not randomly distributed along-axis, but that some underlying process controls not only their emplacement but the initiation of the tectono-magmatic cycle itself.

However, the four distinct stages of the cycle proposed by Parson *et al.* (1993) do not adequately explain all the morphological observations. For example, AVRs are observed that have characteristics of two stages, for example, *adolescent* and *mature*. Therefore, the *young–adolescent–mature-old* stages merely reflect snapshots in a continuous life cycle, whereby an AVR gradually evolves from one stage to the next, incorporating features characteristic of each stage in the transition process.

The existence of a symmetrical and systematic along-axis age pattern implies that melt is not supplied to each AVR independently from the mantle in some random or chaotic manner, but is instead more centrally focused within an ∼70 km lateral distance encompassing multiple AVRs.

## 5 GRAVITY MODELLING

The hypothesis that the relative age of AVRs should be reflected in their crustal structure can be tested. Having established a relative AVR age chronology, the crustal structure of each AVR may be modelled from gravity data, using the RAMSSES AVR to constrain and ground-truth this modelling process.

Before modelling the shorter-wavelength (∼10 km) gravity anomalies associated with individual AVRs, the longer-wavelength along-ridge anomaly, or 'regional' field, must first be characterized to determine the nature and extent of Iceland hotspot influence and confirm the underlying assumption that 59°N marks the southernmost boundary of hotspot influence. Consequently, an average layered crustal model may be developed for the axial region and the residual mantle Bouguer anomaly calculated. By correlating the variation in residual mantle Bouguer anomaly between AVRs, the shorter-wavelength (in geophysical terms) variation in crustal structure may be considered in the context of AVR morphology and relative age.

### 5.1 Along-axis FAA—hotspot-related crustal structure

An ∼650-km-long profile was extracted from the FAA compilation and modelled using *gravmag* (British Geological Survey—Pedley *et al.* 1993). A three-layer (sea water, crust, mantle) approach was adopted since the along-axis variation in layer 2A and 2B thickness and density primarily results in only shorter-wavelength (<10 km) gravity anomalies, which are assumed to largely correlate with layer 2 variation only.

Initial crustal layer densities were obtained from the RAMESSES gravity models (Navin *et al.* 1998) and are summarized in Table 1 (see also Nafe & Drake 1957, 1962; Carlson & Raskin 1984). Throughout this paper densities are quoted in g cm$^{-3}$ for brevity of annotation on figures—1 g cm$^{-3}$ is equivalent to 1000 kg m$^{-3}$. Modelling was also constrained using all available zero-age crustal thickness determinations from the Reykjanes Ridge as a whole (± 1.0 km in all cases) of 7.5 km, 8.0 km and 10.0 km obtained from seismic models at 57°45′N, 59°30′N and 61°40′N respectively (Bunch & Kennett 1980; Smallwood *et al.* 1995; Navin *et al.* 1998, respectively and see Fig. 6).

**Table 1.** Initial gravity model layer densities using average *P*-wave velocities derived from the main layers of Navin *et al.'s* (1998) across-axis wide-angle seismic model. *Vp*—average *P*-wave velocity of each layer, $\rho_{nd}$—density from the Nafe & Drake (1957) relationship, and $\rho_{m2}$ and $\rho_{m3}$—densities from method 2 and 3 respectively of Carlson & Raskin (1984). The average, $Av_\rho$, of these three methods is shown for reference. The mantle is represented by a density of 3.30 g cm$^{-3}$, common to many ridge gravity studies (e.g. Kuo & Forsyth 1988; Cormier *et al.* 1995). The main difference between the two methods of Carlson & Raskin (1984) is that method 3 attempts to take into account the large-scale porosity encountered in oceanic layer 2A.

| | | Nafe & Drake (1957) | Carlson & Raskin (1984) | | | Navin *et al.* (1998) | 3-layer initial model |
|---|---|---|---|---|---|---|---|
| | *Vp* (km s$^{-1}$) | $\rho_{nd}$ (g cm$^{-3}$) | $\rho_{m2}$ (g cm$^{-3}$) | $\rho_{m3}$ (g cm$^{-3}$) | $Av_\rho$ (g cm$^{-3}$) | (g cm$^{-3}$) | (g cm$^{-3}$) |
| water | 1.49 | — | — | — | 1.03 | 1.03 | 1.03 |
| sediments | 2.60 | 2.10 | 1.51 | 2.04 | 1.89 | 1.60 | |
| layer 2A/B | 5.00 | 2.54 | 2.61 | 2.74 | 2.63 | 2.40/2.53 | 2.75 |
| layer 3 | 6.75 | 2.89 | 2.92 | 2.94 | 2.92 | 2.85 | |
| mantle | 8.00 | 3.26 | 3.06 | 3.03 | 3.11 | 3.30 | 3.30 |

Apart from seabed topography, which contributes significantly to the observed field, there are a number of potential causes of variation of the observed FAA:

(1) crustal thickness variation;
(2) density variation in the crust;
(3) density variation in the upper mantle and
(4) any combination of any of the aforementioned causes.

Only variations in crustal thickness (Fig. 6b), upper mantle density (Fig. 6c) and a combination of crustal thickness and upper mantle densities (Fig. 6d) are considered, as seismic observations suggest that these are the most likely manifestation of the longer-wavelength effects of the Iceland hotspot on the along-axis structure of the ridge as a whole. Variations in density within the crust along-axis are generally shown to be the source of the shorter-wavelength anomalies, which reflect the pattern of segmentation or morphological variation at a subsegment level.

Starting with the simplest case, if a constant crust and upper mantle density are assumed (Fig. 6b) then solely an increase in crustal thickness from 7.0 km at 57°45′N to ∼11.5 km at 61°40′N, results in an anomaly fit. However, this model does not fit the seismic crustal thickness determinations of Bunch & Kennett (1980) at 59°30′N nor, if extended further north, the estimate of Weir *et al.* (2001) near 62°40′N.

Similarly, assuming a constant crustal density and thickness, a decrease in upper mantle density from 3.30 g cm$^{-3}$ at 57°45′N to 3.14 g cm$^{-3}$ near 62°N (Fig. 6c), also fits the observed anomaly. This model, when extrapolated further north, is not compatible with the observations of Weir *et al.* (2001) both in terms of overall crustal thickness and upper mantle density, 11.0 km and 3.23 g cm$^{-3}$, respectively, at 62°40′N.

The preferred model, presented in Fig. 6(d), provides a good fit to the observed FAA and all available crustal thickness and upper mantle density determinations. The generally quoted normal oceanic crustal thickness of 7.1 ± 0.8 km of White *et al.* (1992) (dashed lines in Figs 6b–d) is only exceeded north of 59°N, which suggests that crustal thickness in TOBI area C is not significantly influenced by the Iceland hotspot.

Note that the shorter-wavelength (∼10 km) free-air anomalies are not adequately modelled (within seismic constraints) indicating that, as already proposed, smaller-scale along-axis variations in intracrustal layer thickness, and probably density, are the prominent source of these observed anomalies.

Although the preferred model is rather simplistic it does allow a number of conclusions to be drawn. Firstly, the AVRs which comprise TOBI area C lie at, or beyond, the limit of any significant hotspot influence on crustal thickness. Consequently their accretionary processes and magma supply are unlikely to be affected by any significant increase in melt generation rates or thermal flux associated with the hotspot. As observed in Section 3.2 (Fig. 4b), the FAA increases in value heading northwards towards Iceland, which suggests that the elevated topographic bulge associated with the Iceland hotspot is not in complete isostatic equilibrium. This modelling suggests that the bulge is partly isostatically compensated both by a decrease in mantle density and by an increase in crustal thickness heading towards the hotspot centre, but that dynamic forces associated with the underlying plume must also contribute to the overall topographic signature of the hotspot.

### 5.2 Along-axis residual mantle Bouguer anomaly—AVR-related crustal structure

To determine the variation in crustal thickness and density associated with individual AVRs and to investigate whether AVRs in their magmatic phase are also related to density anomalies in the crust and mantle associated with melt ascent and its accumulation within the crust, the mantle and residual mantle Bouguer anomalies (MBA and RMBA, respectively) were calculated. The MBA is equivalent to the FAA corrected for the 3-D effect of seabed topography assuming a constant density and thickness layered crustal structure model (Prince & Forsyth 1988). The MBA thus reveals any anomalous density regions or variations in crustal layer thickness relative to that model. The RMBA is the result of further correcting for thermal-related density changes in the mantle due to passive mantle upwelling at the ridge axis and subsequent plate cooling (Phipps Morgan & Forsyth 1988, after Forsyth & Wilson 1984). The MBA and RMBA are more appropriate than the FAA for studying individual AVRs and their interrelationships, since the gravitational effects of the density contrast across the sea water–seabed interface (which contributes ∼70 per cent to the total field and hence masks the smaller-scale anomalies associated with the variation in crust and mantle properties of interest here) are fully accounted for.

The simple crustal model used to calculate the MBA consists of constant thickness and density layers—set in the context of the geophysical definition of oceanic layers 2A, 2B and 3—and a constant density mantle draped beneath the seafloor topography (see Fig. 7 and Table 2 for details). Layers 2A and 2B are included in this model because their across-axis variation would be expected to contribute significantly to the gravity anomaly at the AVR scale. However, the

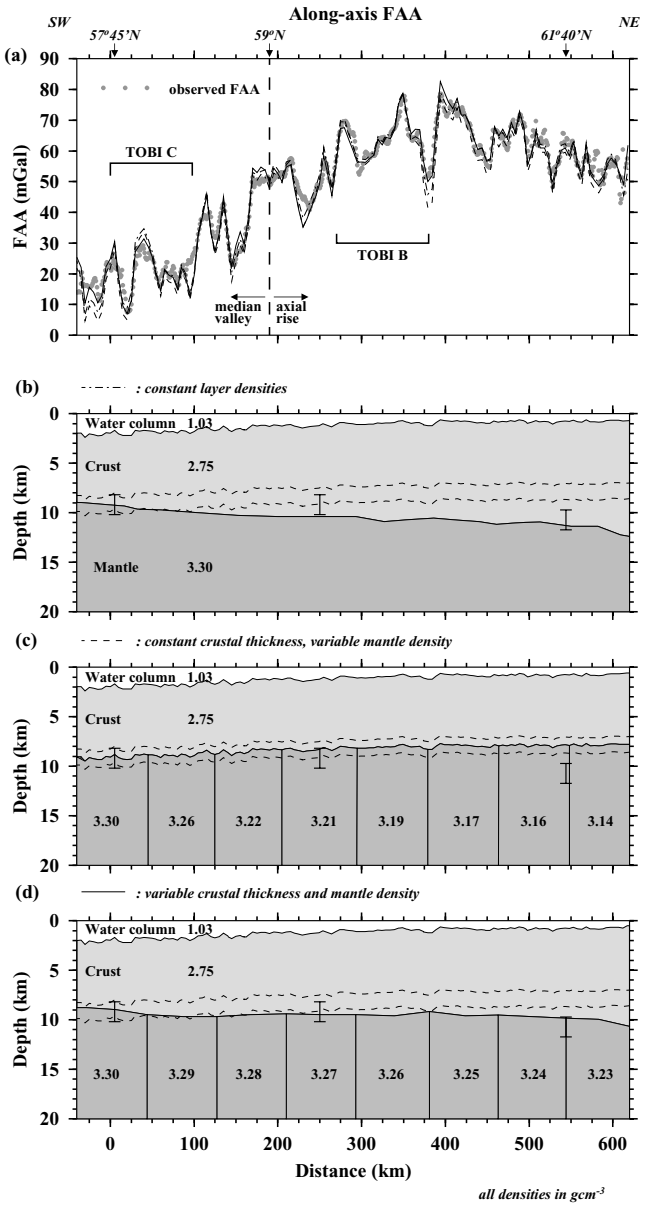


**Figure 6.** Influence of the Iceland hotspot on crustal structure. (a) Calculated (dashed and solid lines) and observed (dots) free-air gravity anomalies along-axis from 57°30′N to 62°12′N. (b) Constant density model showing how the crust would have to reach a thickness of ∼12 km at 62°N to match the observed anomalies in the absence of any mantle density variation. (c) Model showing mantle densities required to match the observed anomalies assuming no crustal thickening. (d) Model fitting all available seismic crustal thickness and mantle density determinations, consisting of variable crustal thickness and mantle density, with an increase in crustal thickness and a gradual decrease in mantle density towards Iceland. Error bars show the seismic crustal thickness determinations of various authors (see text). Dashed lines within models show White *et al.*'s (1992) 'normal' oceanic crustal thickness of 7.1 ± 0.8 km.

average crustal density and thickness is equivalent to that of the FAA modelling results shown in Fig. 6.

For the MBA, the approach of Prince & Forsyth (1988) was adopted as described in detail in Peirce & Navin (2002). To enable the MBA calculation to be performed on a regular grid of nodes (see Table 2), the bathymetry grid was rotated though 36° to align the

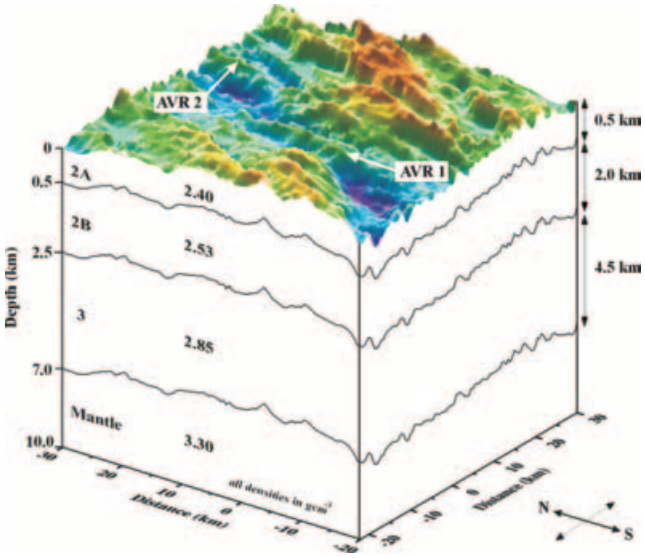


**Figure 7.** Example from the simple crustal model used for the MBA calculation. Layers of constant density and thickness are draped beneath the seafloor topography. The thickness and density of each layer are annotated.

oblique trend of the ridge in a 'north–south' direction. The resulting MBA is shown in Fig. 8(a).

The MBA amplitude on-axis (Fig. 8a) follows a linear trend heading northwards from ∼45 mGal at 57°25′N to −10 mGal at 62°N, an along-axis gradient of 0.095 mGal km$^{-1}$, with peak-to-trough amplitudes of 1–10 mGal. A number of AVRs display the 'bull's eye' pattern, with anomaly lows at segment centres, similar to those observed elsewhere on the MAR (e.g. Kuo & Forsyth 1988; Lin *et al.* 1990; Tolstoy *et al.* 1993; Detrick *et al.* 1995), although their amplitudes are much smaller. The local anomaly highs over the inter-AVR basins suggest the presence of thinner crust (Searle *et al.* 1994a). The general northwards decrease in anomaly supports the conclusion that the crust thickens and/or mantle densities decrease towards Iceland relative to the crustal model used to calculate the MBA (*cf*. Fig. 6d). The small along-axis gradient and low 'bull's eye' anomaly amplitudes suggest that the strong 3-D pattern of upwelling that is observed at other slow-spreading ridges is subdued at the scale of individual AVRs at the Reykjanes Ridge, resulting in an MBA pattern more akin to faster-spreading ridges (Lin & Phipps Morgan 1992; Cormier *et al.* 1995; Magde *et al.* 1995). The MBA also follows the ridge trend rather than the AVR trend. In addition, the lack of prominent 'bull's eye' lows associated with individual AVRs and the observed longer-wavelength ridge-parallel anomaly, which encompasses several adjacent AVRs, suggests that the segmentation pattern associated with melt supply may also be operating over a larger length-scale than that of individual AVRs—that is, that a segment here comprises several AVRs.

To calculate the RMBA, the thermal effect of passive upwelling at the ridge (Phipps Morgan & Forsyth 1988) is subtracted from the MBA (Fig. 8b). The change in ridge trend near 59°N (Fleischer 1974) and the individual AVRs were accommodated by subdividing the ridge into a series of short segments each offset by transforms. Although transform offsets do not exist between AVRs in reality, the short offset distances involved in this assumption do not contribute significantly to the resulting anomaly pattern, and thus this representation is considered to be acceptable within errors.

The RMBA (Fig. 8c) still shows a decrease in anomaly amplitude towards Iceland and the 'bull's eye' lows associated with

**Table 2.** Definition of parameters used during gridding and the individual stages of the RMBA calculation.

| | Parameter | Value |
|---|---|---|
| General | | |
| | Bathymetry grid node spacing (latitude/longitude) | 0.12′/0.06′ (or 0.2 km/0.2 km) |
| | Spreading half rate | 10 mm $yr^{-1}$ |
| | Resampled and rotated bathymetry: | |
| | number of samples in x | 512 |
| | number of samples in y | 2 × 1024 |
| | node spacing in x | 0.2 km |
| | node spacing in y | 0.2 km |
| MBA | | |
| | Number of model layers | 4 |
| | Densities of layers: | |
| | water | 1.03 g $cm^{-3}$ |
| | 2A | 2.40 g $cm^{-3}$ |
| | 2B | 2.53 g $cm^{-3}$ |
| | 3 | 2.85 g $cm^{-3}$ |
| | mantle | 3.30 g $cm^{-3}$ |
| | Thickness of layer beneath seabed: | |
| | 2A | 0.5 km |
| | 2B | 2.5 km |
| | 3 | 4.5 km |
| RMBA | | |
| | Thermal expansion coefficient | $3.4 \times 10^{-5}$ $°C^{-1}$ |
| | Gravitational constant | $6.673 \times 10^{-11}$ N $m^2$ $kg^{-2}$ |
| | Plate thickness | 100 km |
| | Asthenospheric temperature | 1350°C |

individual spreading segments, confirming that the MBA observations are due to either variations in crust and/or mantle density or crustal thickness. From 57°30′N to 58°30′N a number of 2–5 mGal RMBA highs coincide with second- and third-order discontinuities (Fig. 9).

Removal of the long-wavelength linear along-axis trend (see Figs 9 and 10) further highlights AVR-scale positive and negative relative anomalies, with a broad RMBA low of ∼2 mGal following the ridge-trend. This observation provides further support to Peirce & Navin's (2002) conclusion that magma delivery takes place along the ridge trend and that AVRs, created along a spreading-orthogonal direction, tap into this broad ridge-trending upwelling. A number of small 'bull's eye' lows are visible along the ridge axis. A −6 mGal low is associated with AVR 1 while further north AVR 2 has instead a −1 mGal low located towards the southwest. The next 'bull's eye' low of −4 mGal, occurs over AVR 4. Anomalies then generally decrease in amplitude, culminating with a small −3 mGal low over AVR 7. Off-axis traces of RMBA lows over AVRs 1, 2, 4 and 6 are asymmetric, suggesting variations in relative crustal structure on either side of the ridge axis. These observations are interpreted to reflect asymmetry in the crustal accretion process itself, and this interpretation will be tested by calculating local spreading rates in Section 7.

## 6 TECTONO-MAGMATIC CYCLES AND CRUSTAL STRUCTURE OF AVRS

If crustal structure is intimately related to melt supply, AVRs ageing through the magmatic phase of their life cycle should have a correspondingly thicker crust and/or lower density within the crust when compared with those either undergoing tectonic extension or at the beginning of their life cycle. To investigate if such a correlation between crustal structure and AVR age exists, the shorter-wavelength AVR RMBAs were modelled in 2-D (Fig. 10). Although the crustal structure of an AVR is unlikely to be 2-D, the 2-D assumption is valid for mid-crustal features with a half-strike length greater than 5 km (Gardiner 2003) largely because the RMBA calculation removes the affect of the seabed topography, which accounts for ∼70 per cent of the gravity anomaly and represents by far the majority of the in- and out-of-plane variability. A four-layer model (Fig. 11), based on the RAMESSES model of Navin *et al.* (1998) and consisting of oceanic layers 2A, 2B, 3 and the upper mantle, was used as an initial starting point for all AVRs.

### 6.1 AVR 1 (RAMESSES)

The crustal structure models for AVR 1 (Fig. 11) are taken from Peirce & Navin (2002) and are included for purposes of comparison and ground-truthing with models for the other AVRs presented here, which are based solely on gravity modelling. Peirce & Navin (2002) interpret the low-density region in layer 3 as containing a high percentage of partial melt, with the lowest density block, off-centre but beneath the shallowest topography, representing the region of most recent melt influx. This conclusion is supported by MacGregor *et al.*'s (1998) analysis of coincident CSEM data which suggests up to 20–40 per cent melt may be present. Note that an ∼100-m-thin melt lens, identified by the seismic modelling of Navin *et al.* (1998), has been included in the AVR 1 gravity models for completeness only as it does not give rise to a significant gravity anomaly within the resolution of the data.

### 6.2 AVR 2

The along-axis RMBA (Fig. 12) has no distinct low associated with the segment centre, instead small fluctuations of ∼1mGal on a ∼5 km length scale occur around a 1 mGal background average. A simple crustal structure with constant densities and thinning of ∼200 m (Fig. 12c) results in an acceptable fit, while a mid-lower crustal density distribution such as that modelled for AVR 1 (Fig. 12d) produces a large misfit (∼5 mGal). The best fit is achieved with small variations in layer 2 thickness (200–400 m) and no crustal thinning (Fig. 12e). A −1 mGal RMBA low, slightly off-axis to the southwest of this AVR (see Fig. 10), may indicate its continued growth/rejuvenation via off-axis melt migration, or that a new influx of melt to the crust is leading to the initiation of a new AVR.

### 6.3 AVR 4

This AVR has longer-wavelength RMBA variations (∼10 km) similar to that of AVR 1 but the anomaly amplitude only reaches a relative −4 mGal low at the segment centre (Fig. 13). Small variations in layer 2 thickness, in a crustal structure with no mid-lower crustal density variations and no crustal thinning (Fig. 13b), match the shorter-wavelength features of the RMBA only. Combining variations in layer 2 thickness with crustal thinning of ∼400 m towards the segment ends (Fig. 13c) produces a better overall fit, but including the mid-lower crustal densities of AVR 1 into the model (Fig. 13d) results in a 3 mGal misfit. However, reducing the densities in the mid-lower crust beneath the segment centre by only 0.01–0.03 g $cm^{-3}$ (Fig. 13e) produces the best fit and would indicate the presence of 5–15 per cent retained melt (Hooft & Detrick 1993). Crustal models with either an increase in crustal thickness beneath the AVR-centre or the presence of a small amount of partial

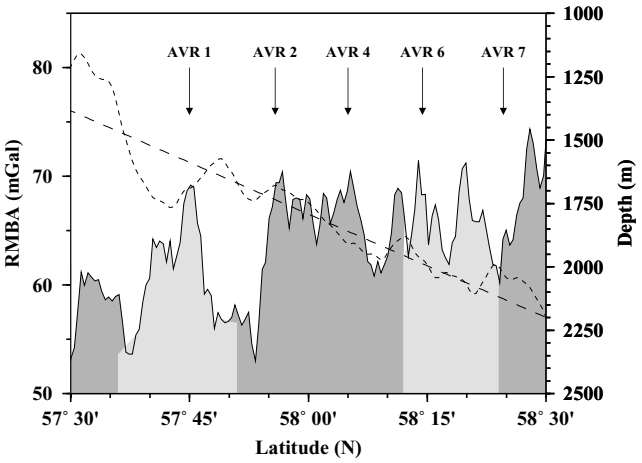


**Figure 9.** Along-axis profiles of bathymetry and RMBA for TOBI area C. The bathymetry (solid line) shows short-wavelength variations associated with individual AVRs (annotated arrows) and intermediate-wavelength variations associated with segment discontinuities. Segment boundary locations are from Applegate & Shor (1994) and are shaded in grey. The RMBA profile (dotted line) is superimposed together with its long-wavelength trend (dashed line). Note how bathymetry highs are generally associated with relative RMBA lows.

melt in the mid-lower crust are both consistent with the relatively *mature* age of this AVR.

### 6.4 AVR 6

This AVR is characterized by a −1 mGal RMBA low at its centre (Fig. 14). Models with: variations in layer 2 thickness of up to 500 m (Fig. 14b), crustal thinning of ∼1 km to the south and of ∼500 m to the north of the segment centre (Fig. 14c), or a 0.03–0.04 g cm$^{-3}$ density anomaly (15–20 per cent partial melt) in layer 3 beneath the segment centre (Fig. 14e) all produce an acceptable fit. Density anomalies in the mid-lower crust similar to those modelled for AVR 1 (*cf.* Fig. 11e and Fig. 14d) produce a 5 mGal misfit (Fig. 14d). A crustal model suggesting more partial melt in the crust than AVR 4 (Fig. 13e) is consistent with the *young* to *adolescent* age of this AVR and also, more significantly, that an influx of melt may have occurred relatively recently.

### 6.5 AVR 7

This AVR has short-wavelength RMBA variations of ∼5 km and only reaches a −3 mGal low over the segment centre (Fig. 15). The along-axis crustal structure can be modelled in several ways that all produce acceptable fits to the RMBA: a slightly thicker (∼500 m) layer 2 beneath the segment centre (Fig. 15b), crustal thinning of ∼1 km towards the ends of the profile, with smaller variations in layer 2 thickness (Fig. 15c), or more subdued variations in crustal and layer 2 thickness with a 0.01–0.02 g cm$^{-3}$density anomaly, equivalent to 5–10 per cent retained melt, in the mid-lower crust beneath the segment centre (Fig. 15e). Fig. 15(d) shows that mid-lower crustal densities as low as that modelled for AVR 1 would produce a significant misfit. A model with less partial melt in the crust than AVR 6 is consistent with its interpreted *adolescent* age.

### 6.6 Layer 2A and 2B density variations

All of the along-axis AVR models have layers 2A and 2B with densities of 2.40 g cm$^{-3}$, in common with the RAMESSES model of Navin *et al.* (1998), as little layer 2A and 2B density variations are

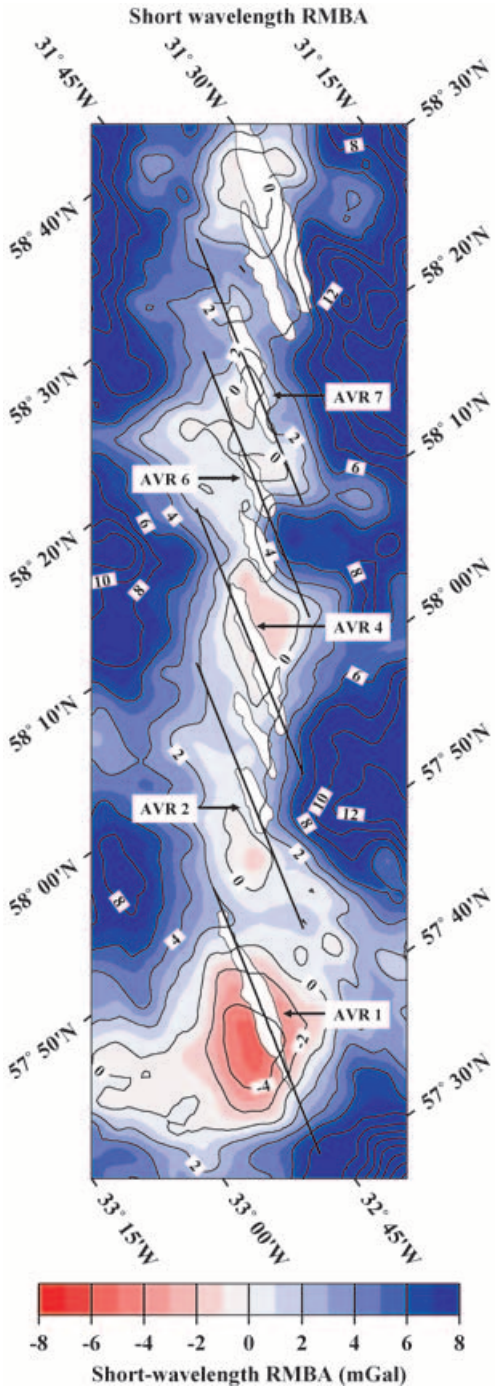


**Figure 10.** RMBA with the linear 'regional' trend shown in Fig. 9 removed to highlight AVR-related features. A broad low follows the ridge trend with small 'bull's eye' lows associated with a number of AVRs superimposed. Solid lines show the profiles extracted to model the crustal structure of the selected example AVRs (see Figs 11–15). AVR footprints are superimposed in white for clarity and the chosen example AVRs labelled. Contours are plotted at 2 mGal intervals.

expected for near zero-age crust. However, the effect of density variations in layers 2A and 2B should investigated (Fig. 16) to provide constraint on their resolvability and to test the assumption that the RMBA lows do not have an origin in layer 2 alone.

The upper crustal structure of the only model (AVR 1—Fig. 11e) whose layer boundaries are constrained by seismic data provides the

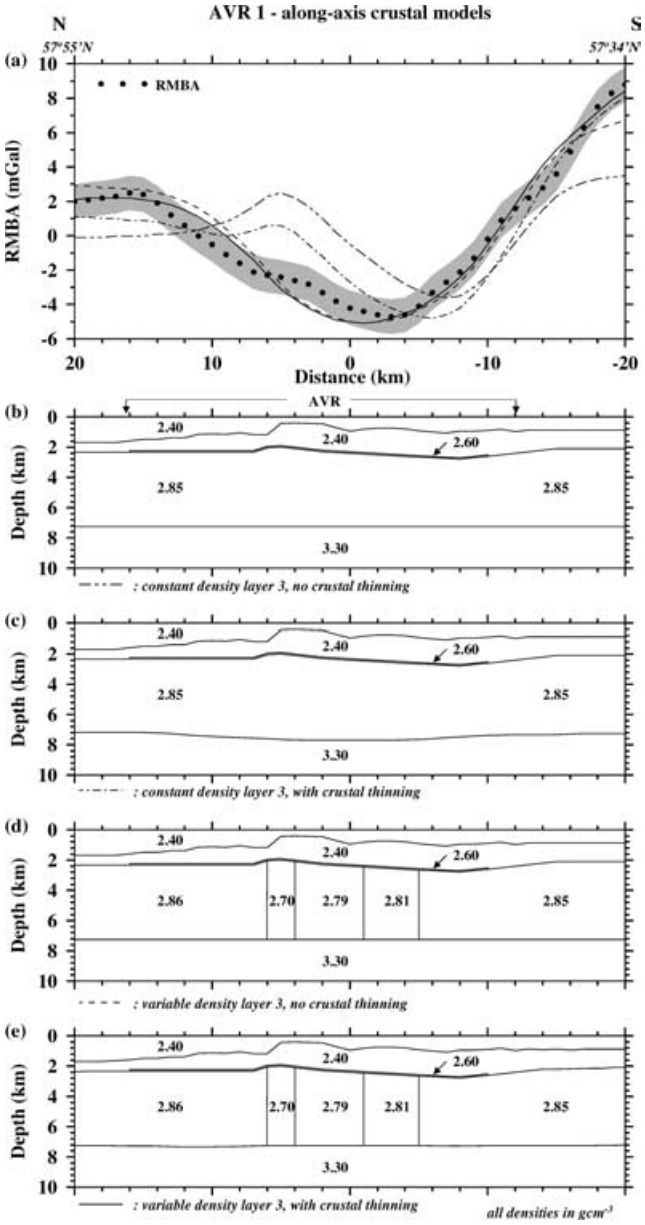


**Figure 11.** Along-axis RMBA profile for AVR 1 sampled from the short-wavelength RMBA plot of Fig. 10. The RMBA is shown by dots, with error bounds (grey shaded region) and calculated anomalies for each of the models shown in (b)–(e) superimposed. Models include layers 2A, 2B, 3 and the upper mantle. The lateral extent of the AVR is highlighted. (b)–(e) explore the contributions to the RMBA of variations in crustal thickness, variations in mid-crustal densities, and combinations of crustal thickness and mid-crustal density variations. A crustal model that includes a low-density region towards the centre of the AVR and crustal thinning towards AVR tips results in the best fit. Note the crustal thinning in (e) is only ∼200 m over the entire length of the AVR.

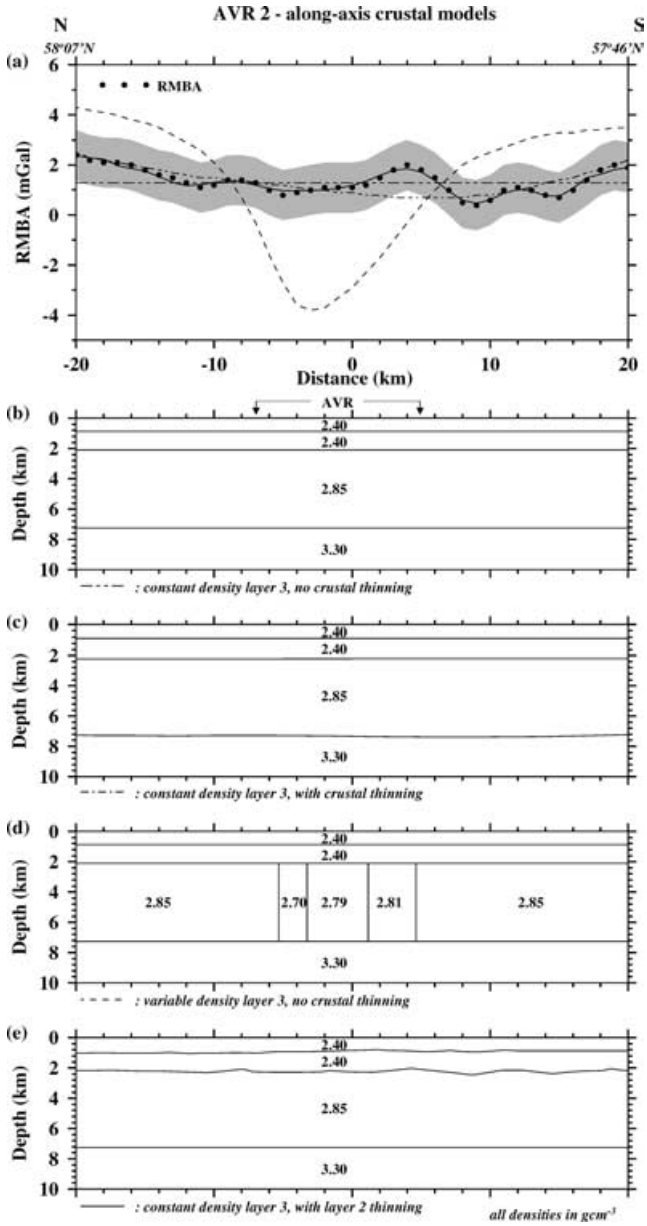


**Figure 12.** Along-axis RMBA profile for AVR 2. See Fig. 11 for details. The RMBA can be satisfactorily matched by models comprising constant density layers with little-to-no crustal thinning towards the AVR tips. Small variations in layer 2 thickness can account for the shorter-wavelength features of the RMBA. Note the crustal thinning in (c) is only of the order of 200 m over the entire length of the AVR.

starting point. Increasing layer 2B density to 2.53 g cm$^{-3}$, a density generally ascribed to off-axis layer 2B (Navin *et al.* 1998), results in a misfit, especially at the northern end of the AVR (Fig. 16c). In fact, if layer 2B density is 2.53 g cm$^{-3}$ its thickness would have to be halved to produce an acceptable fit. Introducing a gradational change (Fig. 16d), from 2.40 g cm$^{-3}$ at the AVR centre to 2.53 g cm$^{-3}$ at the AVR extremities, slightly improves the fit at the northern end of the AVR but does not fit the whole profile unless significant variation in thickness is also included. Combining gradational changes in densities of layers 2A and 2B (Fig. 16e) from 2.40 g cm$^{-3}$ at the AVR centre to 2.45 g cm$^{-3}$ and 2.53 g cm$^{-3}$ at the AVR extremities, respectively, results in a good fit to the observed RMBA at the northern end of the AVR. However, the fit for the rest of the profile is not within the error bounds.

Thus, this layer 2A and 2B density variation sensitivity modelling precludes large variations in density without having to significantly alter the seismically constrained layer thicknesses as well. However, subtle layer 2A and 2B density variations of ∼0.05 g cm$^{-3}$ are not precluded but these cannot account for the AVR-centred RMBA lows alone.

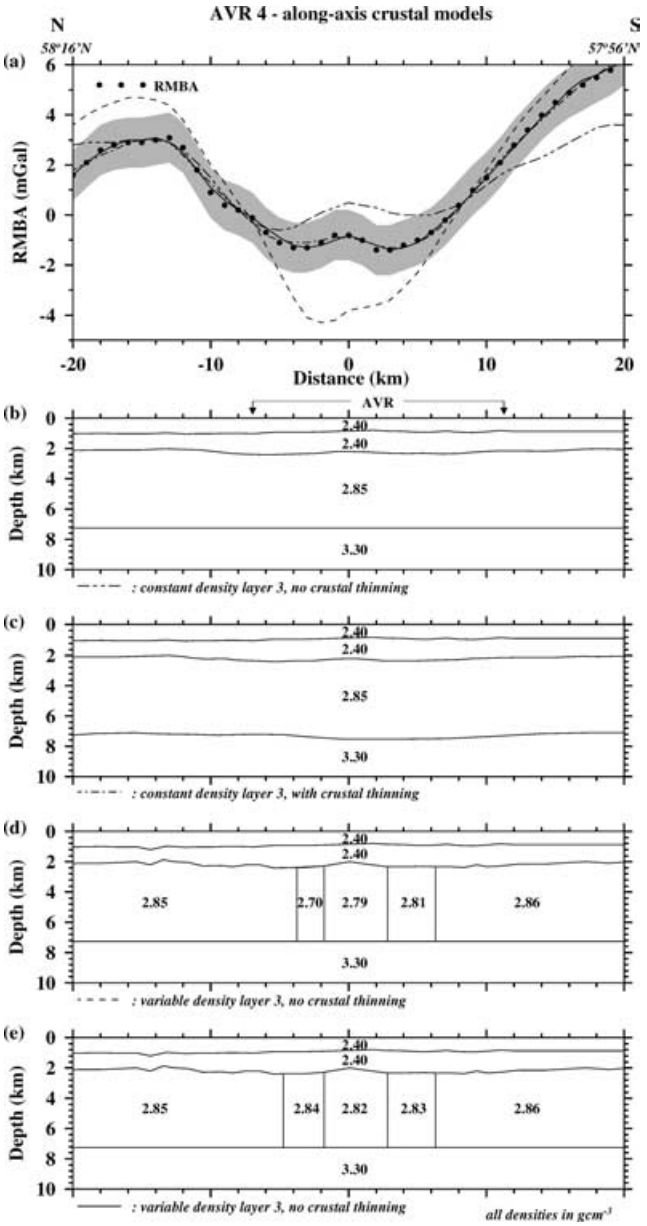


**Figure 13.** Along-axis RMBA profile for AVR 4. See Fig. 11 for details. Models with constant density layers and crustal thinning towards AVR tips, or with a low-density region in the mid-crust beneath the centre of the AVR produce a reasonable fit.

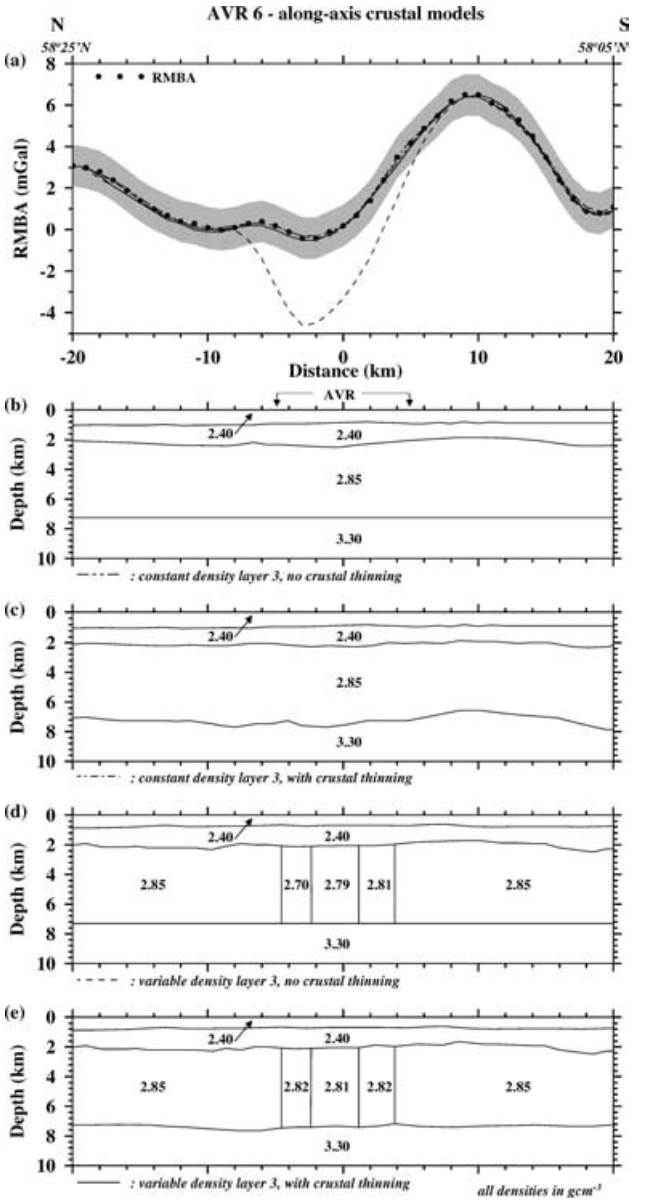


**Figure 14.** Along-axis RMBA profile for AVR 6. See Fig. 11 for details. The RMBA can be matched by variations in layer 2 thickness alone, variations in crustal thickness, or by a low-density region in the mid-crust together with crustal thinning towards the AVR tips.

### 6.7 Upper mantle contributions

The RMBA profiles have all been modelled assuming that the observed anomalies result from variations in crustal thickness and/or density. However, another possible source of the RMBA lows are mantle density variations due to melt retention, thermal expansion and compositional changes caused by the extraction of partial melt (although compositional density reductions in the mantle are unlikely to contribute significantly to the observed gravity anomaly—Magde *et al.* 1995). Although the 2-D modelling presented here cannot differentiate between the different possible sources of low density in the upper mantle it can help constrain possible models for mantle plumbing, that is, how the melt ascends from the source region in the mantle to the crust.

To investigate possible models of mantle plumbing AVR 4 was selected as it is associated with an RMBA low and crustal modelling suggests that only a small density anomaly in layer 3 is required to explain it. To test if this low can equally be explained by density variation in the mantle, the crustal model of AVR 4 (Fig. 13c) was used as a starting point, with the upper mantle extended to 80-km-depth bsl and a region of lower densities incorporated beneath the AVR centre to investigate different conduit geometries and melt retention models. Density anomalies were converted to percentages of retained melt assuming a density contrast of 0.5 g cm$^{-3}$ between basaltic melt and peridotite (Sparks *et al.* 1993). Modelling shows that a mantle model with an ∼10 km wide conduit extending to a depth of 80 km bsl, with more than 4–8 per cent retained melt, results in a significant misfit (Fig. 17a). However, by reducing the amount of retained partial melt in the conduit to ∼0.5 per cent a

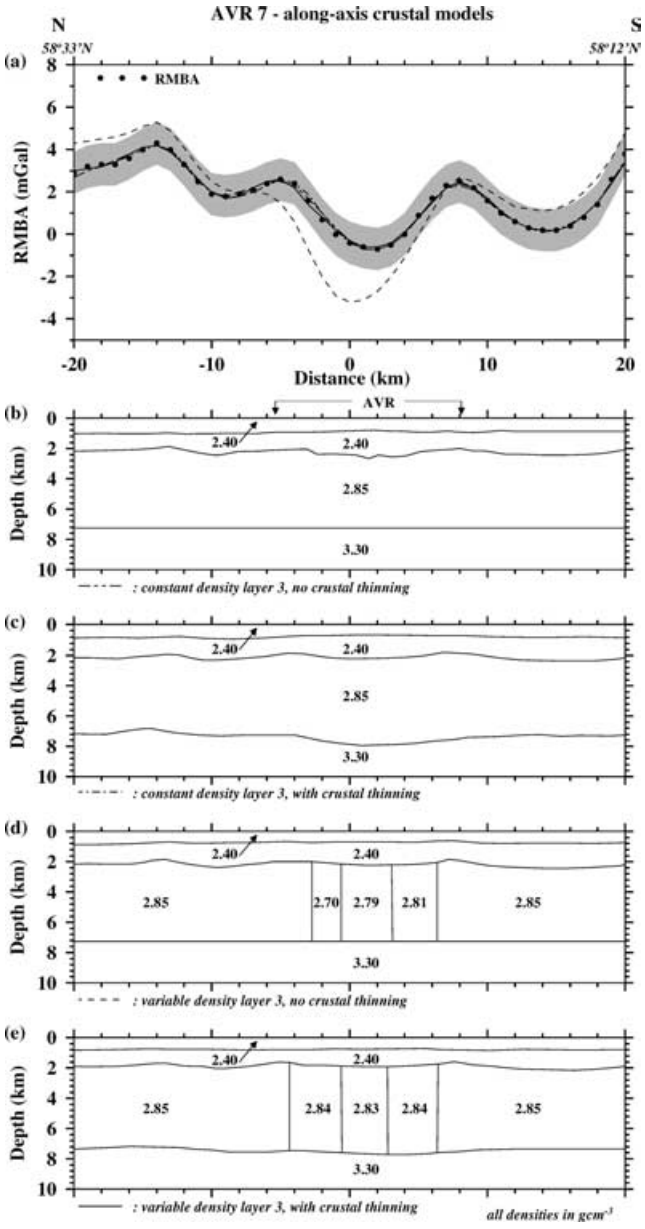


**Figure 15.** Along-axis RMBA profile for AVR 7. See Fig. 11 for details. Models with constant density layers and crustal thinning towards the AVR tips, or with a low-density region in the mid-crust and more subdued crustal thinning towards the AVR tips produce a satisfactory fit.

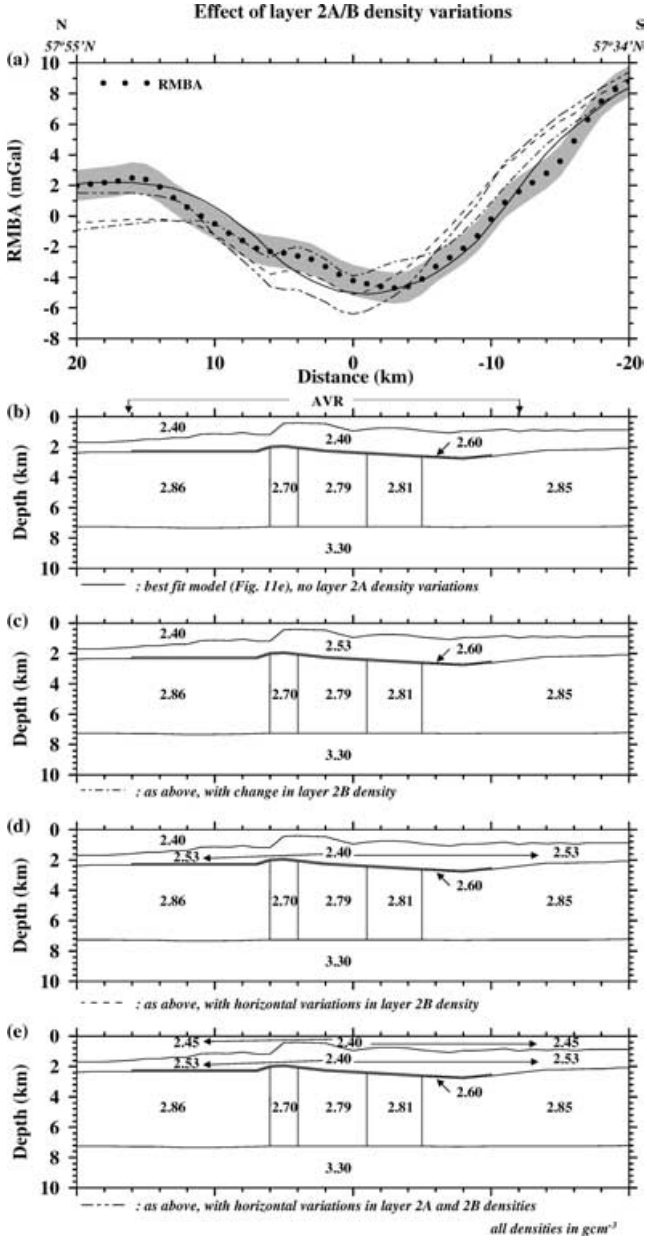


**Figure 16.** Effect of variation in layer 2A and 2B density. (a) Observed (dots) and calculated anomalies with error bounds superimposed (grey shading). (b) Best-fitting model for AVR 1 (see Fig. 11e). (c) Layer 2B density is changed to 2.53 g cm$^{-3}$, typical of off-axis layer 2B density, resulting in a misfit. (d) A gradational change in layer 2B density, from 2.40 g cm$^{-3}$ to 2.53 g cm$^{-3}$, is introduced. The fit to the RMBA is improved from (c) but is still not within the error bounds. (e) Layer 2A density variations are added to the model shown in (d), resulting in a better fit to the RMBA.

more acceptable fit results (Fig. 17b) which suggests that, to retain higher percentages of partial melt, either the conduit is of a smaller vertical extent (e.g. 20 km and 1 per cent—Fig. 17d) or significantly narrower (2 km wide, *c*. 80 km deep, up to 3 per cent retained melt—Fig. 17e).

Modelling suggests that the upper 80 km bsl of the mantle beneath most of the length of this AVR does not contain more than a few percent partial melt throughout, although it also does not support nor preclude retained melt fractions of less than 4 per cent in regions only a few kilometres across down to depths of 80 km bsl or more. However, the MT data of Heinson *et al.* (2000) preclude the presence of partial melt in the upper mantle down to at least ∼50-km-depth bsl beneath AVR 1 (unless it is contained within narrow vertical pipes to which the method is insensitive) and suggests, if anything, that melt is concentrated around 60 km depth.

The RMBA lows observed over individual AVRs are, therefore, most likely explained by a combination of lower crustal densities and/or an increase in crustal thickness. Modelling is also consistent with highly episodic melt extraction from the upper mantle and its influx to the crust (MacGregor *et al.* 1998; Navin *et al.* 1998; Heinson *et al.* 2000; Peirce & Navin 2002) since the mantle beneath the RAMESSES AVR is observed to currently contain less partial melt than the crustal magmatic system. Similar observations have

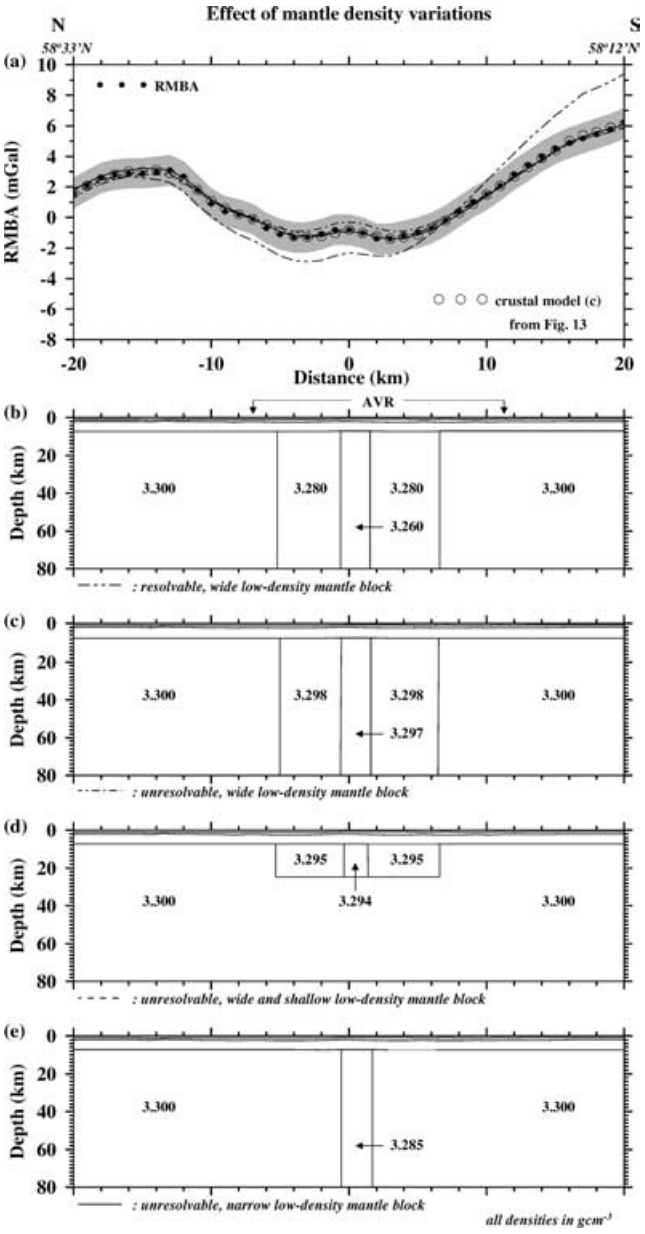


**Figure 17.** Investigation of mantle density variations on the along-axis RMBA of AVR 4. (a) Observed short-wavelength (dots) and calculated (circles) anomaly for the crustal structure shown in Fig. 13(c), and calculated anomalies for each of the models shown in (b)–(e). Models (b)–(e) combine the crustal structure of Fig. 13(c) with various proposed models of upper mantle plumbing. See text for details.

been reported for two segments of the EPR (Magde *et al.* 1995) suggesting that melt injection into the crust is episodic at all spreading rates.

### 6.8 Summary of gravity modelling

The RMBA reveals shorter-wavelength, AVR-centred lows superimposed on a broad ridge-trending low. Gravity modelling shows that a number of these lows can be explained by up to a 1 km thickening of the crust and/or by the presence of low-density regions in the mid-lower crust (see Table 3). Models of crustal structure, showing crustal thickening beneath older and the presence of partial melt beneath younger AVRs, are consistent with the identified stage of each AVR in the tectono-magmatic cycle. Younger AVRs are undergoing magmatic activity with more melt in the mid-lower crust than *mature* AVRs which have reached full crustal thickness and are at the end of their magmatic phase.

AVR 1 is anomalous in that the RAMESSES results indicate it has partial melt within the crust (Navin *et al.* 1998), whereas its long length and *mature* age suggest it should be reaching the end of its magmatic phase with little partial melt remaining. If the hypothesis that tectono-magmatic cycles affect the crustal structure of AVRs is correct, then a likely explanation is that it is undergoing late stage rejuvenation. AVR 2, at ∼10 km in length, is unusually short for its apparent age (*adolescent–mature*). However, an RMBA low off-axis to the west could indicate that its growth is continuing via off-axis melt migration or that the growth of a new AVR has diverted melt flux from it.

The gravity models presented in this section support the theory that tectono-magmatic cycles influence the crustal structure of individual AVRs. In addition, a ridge-trending RMBA low is observed, suggesting that upwelling occurs in this orientation but that melt migrates laterally filling spreading-normal fissures orientated oblique to the ridge direction and forming AVRs (Peirce & Navin 2002). AVRs appear to young and become shorter towards second-order discontinuities, suggesting that AVR growth is initially focussed at the centre of the upwelling and that crustal production gradually extends to the segment extremities.

## 7 MAGNETIC ANOMALY INVERSION AND SPREADING RATE CALCULATIONS

A decrease in magnetization intensity with age, attributed to low-temperature oxidation of titanomagnetite, has been observed at all sampled ridges (e.g. Talwani *et al.* 1971; Johnson & Atwater 1977; Lowrie 1977; Macdonald 1977; Johnson & Hall 1978) with a factor of five reduction in the natural remanent magnetization over the first 0.5 Myr (Johnson *et al.* 1996). Variations in intensity across- and along-axis may, therefore, provide a useful constraint on the relative timing of crustal accretionary processes and allow investigation of asymmetry in spreading that is suggested by the RMBA. Primarily, magnetization intensities will be used to test the relative age of AVRs and to calculate their local spreading rates to determine whether a correlation exists between relative AVR age and local spreading rate. The latter will also be used as a test of the interpretation of the RMBA that spreading may be asymmetric.

The magnetic (Fig. 4c) and bathymetry data (Fig. 4a—Keeton *et al.* 1997) were used to calculate crustal magnetization variations using the 3-D inversion method of Parker & Huestis (1974) and Macdonald *et al.* (1980). Lee & Searle (2000) contains a detailed description of the inversion procedure and the parameters used. Modelling of the calculated magnetization solution reproduces the observed magnetic anomalies to within 1.9 nT rms, indicating that the magnetization intensity solution (Figs 8d and 18) can explain 99.95 per cent of the variance in the magnetic anomaly.

### 7.1 Along-axis—relative AVR age

The highest intensities in the calculated magnetization (Fig. 18) occur along the ridge axis and range from 30 A $m^{-1}$ to 75 A $m^{-1}$. This central anomaly magnetic high (CAMH), which is superimposed on the normal polarity Brunhes anomaly, marks the focus of most recent extrusive activity. Lee & Searle (2000) state that the CAMH is not continuous along-axis on a small scale (<10 km). Instead

**Table 3.** Correlation between relative age, length, RMBA peak-to-trough amplitude and inferred crustal structure for selected AVRs of TOBI area C. The RMBA lows can be modelled by crustal thickening and/or the presence of partial melt in the mid-crust (bold highlighting shows the preferred model, chosen on the basis of the relative age of AVRs). Note that the extent of thickening and the amount of partial melt shown are maximum values and that AVRs 1 and 2 appear to be anomalous.

| Relative age | AVR No. | Length (km) | RMBA (mGal) | Crustal structure | |
|---|---|---|---|---|---|
| | | | | crustal thickening (m) | partial melt |
| *Young–adolescent* | 6 | 11 | −1 | <1000 | **<20 per cent** |
| *Adolescent* | 7 | 20 | −3 | <1000 | **<10 per cent** |
| *Adolescent–mature* | 2 | 10 | −1 (off-axis) | — | — |
| *Mature* | 4 | 35 | −4 | **<400** | <15 per cent |
| *Mature* | 1 | 30 | −6 | <500 | **<40 per cent** |

discrete highs and lows in intensity are associated with AVR-scale features, which appear to be associated with either the age of extrusives and/or variations in layer 2A thickness (assumed to be the magnetic source layer in common with most studies—e.g. Gee & Kent 1994; Hooft *et al.* 1996; Schouten *et al.* 1999; Bazin *et al.* 2001; Fujiwara *et al.* 2003). A magnetization high indicates either the presence of fresher extrusives, more fractionated basalts, a thicker magnetic source layer, or a combination of these different factors.

AVR 1 has the lowest, on-axis average magnetization intensity of ∼35 A $m^{-1}$ for the entire area (Fig. 18). A local magnetization intensity high of 65 A $m^{-1}$ is associated with AVR 2, and the intensities then decrease along-axis to ∼50 A $m^{-1}$ for AVR 4. The intensity magnitude then increases gradually again to 65 A $m^{-1}$ for AVR 6. This pattern of a high over a short AVR, decreasing to a low over a longer AVR, increasing again to a high over a shorter AVR, can be seen further to the north as well.

Lee & Searle (2000) show that no more than 50 per cent of the observed short-wavelength anomaly can be attributed to on-axis layer 2A thickness variations (see also Smallwood *et al.* 1995; Navin *et al.* 1998; Topping 2002). As oxidation of titanomagnetite results in decay of magnetization intensities with age, the shorter-wavelength anomalies can be assumed to reflect local age variations of the extrusive layer. The low magnetization intensity of AVR 1 is unexpected given its relatively young age, although it is consistent with the alternative suggestion that this AVR may be undergoing rejuvenation through late-stage volcanism. A number of small, local magnetization intensity highs associated with small volcanic features along the AVR further support this interpretation.

Another, perhaps simpler, explanation for this observation may be that the highs and lows reflect fractionation trends—with lows reflecting AVRs which erupt relatively less fractionated basalts and the highs corresponding to more fractionated basalts (e.g. Carbotte & Macdonald 1992). Fractionation of basaltic melts results in preferential enrichment of iron and titanium in the melt fraction at the expense of the solid phase, and so can lead to the eruption of lavas which, on cooling, take on stronger remnant and induced magnetizations. Other explanations include the possibility that the magma body beneath AVR 1 is sufficiently large for mixing to effectively inhibit fractionation, resulting in unusually low magnetization intensity basalts or that they were erupted before much fractionation has occurred. Alternatively, hydrothermal activity may have altered the chemical composition of the basalts and reduced the average magnetization intensity. However, German *et al.* (1994), after extensive surveying along the entire length of the Reykjanes Ridge, found no evidence for extensive hydrothermal activity, except for one location, Steinahóll, near the Icelandic coast.

With the exception of AVR 1, a correlation between relative AVR age and average magnetization is observed. Shorter, younger AVRs are associated with magnetization intensity highs, whereas longer, older AVRs exhibit relative lows. The spatial pattern of anomalies, with a gradual increase in magnetization intensity associated with younger, shorter AVRs to the north and south from an older, longer central AVR, supports the suggestion from the TOBI data (Section 4.6) and the gravity modelling (Section 6.8), that a single second-order segment may comprise several AVRs and be of the order of ∼70 km long. This is typical of slow-spreading ridge segments and particularly those of the MAR. In addition, joint consideration of the RMBA, bathymetry (AVR length) and magnetic intensity for the entire ridge axis (e.g. Figs 4 and 8), suggests that this variation repeats at approximately the same interval along its length.

### 7.2 Across-axis—spreading rate variations

Across-axis variation in magnetization intensity, when correlated with a reversal timescale, can be used to calculate spreading rate. Variations in this rate with time may relate to the stage of the AVR in a tectono-magmatic cycle and to the nature of the dominant tectonic process. Tectono-magmatic cycles have been shown in this study to have an effect on the crustal structure of AVRs and it is further hypothesized that the intense magmatic activity associated with AVRs in the *young–adolescent* phase of the cycle may also be reflected in an enhanced local spreading rate relative to *old* AVRs that are simply being dismembered by tectonic processes.

Spreading rates were calculated for profiles orientated in the spreading direction (Fig. 18), using the reversal timescale of Cande & Kent (1995). The slow spreading rate of the Reykjanes Ridge means that the Jaramillo epoch (1.03 Ma) is quite narrow. Half-spreading rate calculations were, therefore, made for each AVR from zero-age to the more prominent reversals at 1.42 Ma between Jaramillo and chron 2 (1.86 Ma) and to chron 2A at 2.81 Ma. Results are shown in Fig. 18 and summarized in Table 4.

In general, longer, older AVRs have slower spreading rates (by up to 20 per cent), for the first 1.42 Ma, than AVRs that are shorter and younger. However, spreading rates for all AVRs, averaged over 2.81 Ma, show little variation within the $\pm 1.0$ mm $yr^{-1}$ error bound. Older AVRs are therefore, simply rafted off-axis at the far-field spreading rate, whereas crustal genesis at younger AVRs enhances the local spreading rate before returning to a 'background' level as magma influx wanes. Similar non-rigid plate tectonic behaviour on short timescales has been reported at 37°N on the MAR (e.g. Macdonald 1977) and at ∼9°N on the EPR (Carbotte & Macdonald 1992), suggesting that independent cycles of magmatic and tectonic activity occur within adjacent segments at all spreading rates. Although these variations are comparable to the error bounds, they are considered significant and supportable given that they mirror both the findings of the TOBI interpretation and gravity modelling.

Spreading rates calculated for the last 1.42 Ma also exhibit asymmetry between the two ridge flanks. However, this asymmetry

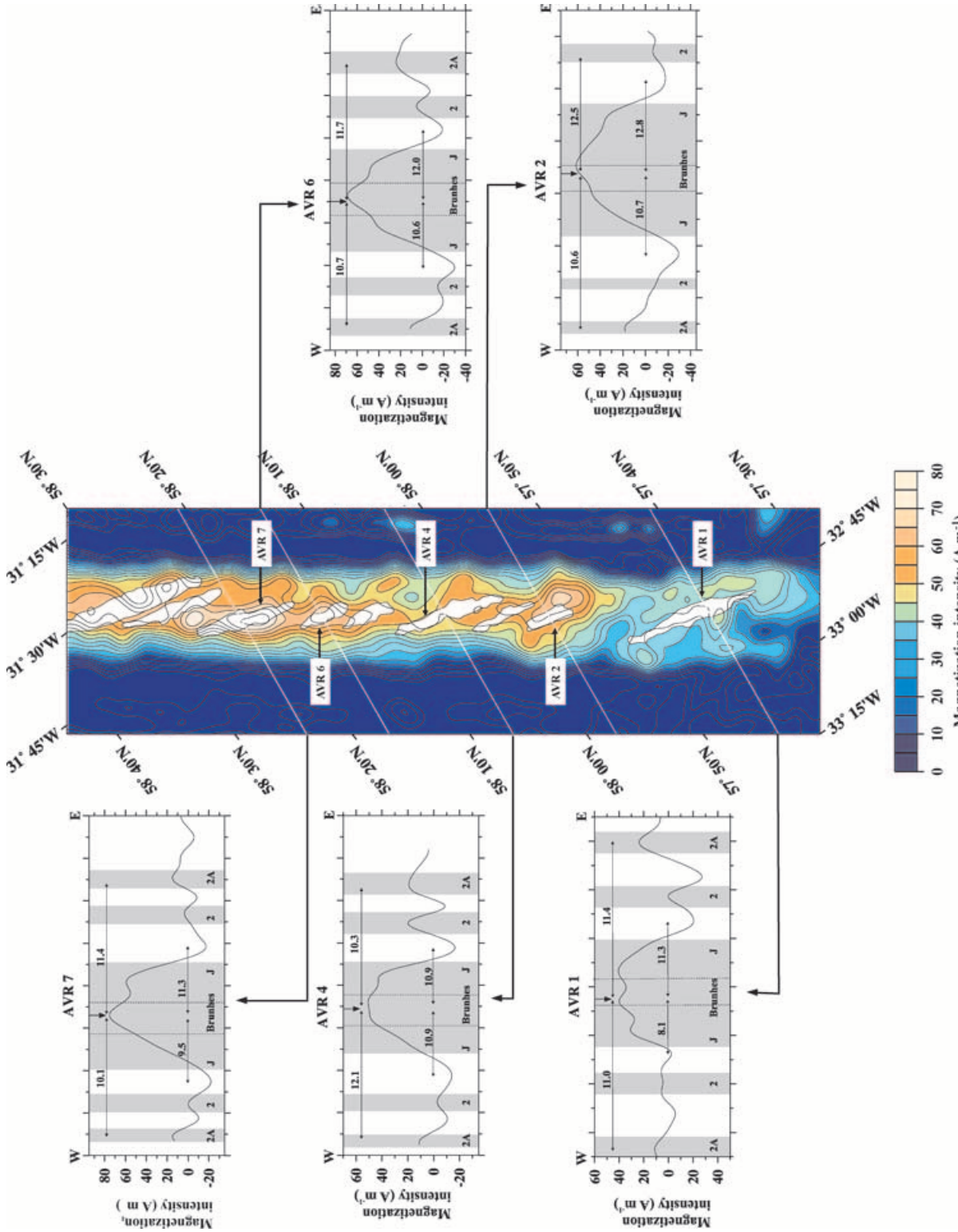


**Figure 18.** Magnetization intensity solution for TOBI area C, showing a number of highs associated with AVRs. AVR 1 is associated with a very low magnetization intensity and appears to be anomalous for this area. AVR outlines are superimposed in white and AVRs selected for spreading rate analysis are labelled and profile lines shown in white. Half-spreading rates were calculated using the reversal timescale of Cande & Kent (1995) between the central high (Brunhes) to the reversal between Jaramillo (J) and chron 2 and to chron 2A. All half-rates are quoted in mm $yr^{-1}$. In all parts, normal polarity epochs are shaded in grey and the vertical arrow and the vertical dashed lines mark the shallowest part and the horizontal extent of the AVR, respectively.

**Table 4.** Correlation between AVR age, length, magnetization intensity and local half-spreading rate across individual AVRs. Longer, older AVRs are generally associated with a magnetization intensity low, whereas shorter, younger AVRs have magnetization highs, confirming the relative age TOBI interpretation. Note that before 1.42 Ma, younger AVRs have higher average spreading rates than older AVRs. However, when averaged over the last 2.81 Ma, spreading rates converge to the average spreading rate for the entire ridge of ∼10 mm $yr^{-1}$. Significant asymmetric spreading rates are shown in bold. AVR ages, obtained from the relative age interpretations of the TOBI data, are abbreviated as follows: *Y − A* for *young–adolescent, A* for *adolescent, A − M* for *adolescent–mature, M* for *mature*.

| Age | AVR | Length (km) | Min. RMBA (mGal) | Mag. Intensity (A $m^{-1}$) | Spreading rate <1.42 Ma (± 0.7 mm $yr^{-1}$) | | | Spreading rate <2.81 Ma (± 1.0 mm $yr^{-1}$) | | |
|---|---|---|---|---|---|---|---|---|---|---|
| | | | | | West | East | Average | West | East | Average |
| *Y–A* | 6 | 11 | −1 | 65 | 10.6 | **12.3** | 11.5 | 10.5 | 11.7 | 11.2 |
| *A* | 7 | 20 | −3 | 75 | 9.5 | **11.3** | 10.4 | 10.1 | 11.4 | 10.6 |
| *A–M* | 2 | 10 | −1(off-axis) | 65 | 10.7 | **12.8** | 11.8 | 10.6 | 12.5 | 11.6 |
| *M* | 4 | 35 | −4 | 50 | 10.9 | 10.9 | 10.9 | 12.1 | 10.3 | 11.2 |
| *M* | 1 | 30 | −6 | 35 | 8.1 | **11.3** | 9.7 | 11.0 | 11.4 | 11.2 |

disappears for spreading rates averaged over 2.81 Ma. Spreading appears to be faster to the east of AVRs 1, 2, 6 and 7 (see Table 4). Although the evidence for asymmetric spreading lies predominantly in the RMBA (see Section 5.2), with RMBA lows located in the direction of slower spreading, those results are supported by the apparent asymmetry in spreading rate even though variation in the latter are comparable to the error bounds. This pattern suggests, assuming off-axis RMBA lows primarily reflect the presence of thicker crust (though crustal and/or mantle density variations may contribute), that differential tectonic extension 'stretches' material accreting to the plate boundary more in one direction than the other. This hypothesis would be supported by evidence for asymmetric faulting, with more faults and/or greater vertical fault offsets to the east within TOBI area C. In fact, although 'flip-flop' style faulting is observed in this area no overall segment-scale asymmetry is obvious and large offsets would be required as the fault scarps are steep (Owens 1991). Alternatively, asymmetry in the crustal accretion process itself may occur, with dykes intruding preferentially to one side of the plate boundary than the other (Macdonald 1977). For example, if a recent intrusion at the ridge axis has sufficient time to cool, the crust at this location may be sufficiently strong such that the next intrusion may preferentially occur somewhere off-axis, along active planes of weakness. The episodic nature of crustal accretion at the Reykjanes Ridge (Navin *et al.* 1998; Sinha *et al.* 1998) may, therefore, also sustain asymmetric spreading.

## 8 DISCUSSION

Gravity and seismic studies suggest differences in mantle upwelling patterns between slow- and fast-spreading ridges (e.g. Kuo & Forsyth 1988; Lin *et al.* 1990; Detrick *et al.* 1995; Magde *et al.* 1995). At slow spreading rates mantle upwelling is thought to be 3-D, with a buoyant diapiric style leading to the formation of small, isolated and ephemeral magma chambers which, in turn, result in the significant variations observed in along-axis crustal structure. At fast-spreading rates, however, 2-D upwelling associated with plate separation dominates. The latter sheet-like pattern of melt delivery results in magma chambers that are largely continuous along the segment length, and in relatively little along-axis variation in crustal structure at the resolution of geophysical imaging. Thus, morphological segmentation at both slow- and fast-spreading ridges can be used as a proxy for the underlying pattern of mantle upwelling and the along-axis extent of individual magma bodies.

However, more recent studies are starting to provide evidence of significant temporal and lateral variability in crustal accretionary processes, and suggest that patterns of alternating phases of tectonic and magmatic activity occur at all spreading rates. Some examples include:

(1) Sauter *et al.* (2002) interpreted TOBI sidescan sonar data collected between 58°20′E and 60°20′E at the very slow-spreading Southwest Indian Ridge (16 mm $yr^{-1}$ full rate) to show that either multiple magma sources exist or that magma is redistributed along-axis through lateral dyke injection.

(2) Lawson *et al.* (1996) interpreted extensive TOBI, deep-towed camera and geochemical data from two segments in the MARNOK area (Mid-Atlantic Ridge North of Kane) to show that variations in apparent age between and within adjacent segments may be due to the episodicity of magma supply and the along-axis migration of melt, respectively.

(3) Sohn *et al.* (1997) interpreted data from a 3-D tomography experiment over the intermediate-spreading (60 mm $yr^{-1}$) Co-axial segment of the Juan de Fuca Ridge to show that the along-axis velocity structure indicates a shift from magmatic to amagmatic extension and reflects variations in magma supply along-axis.

(4) Karson *et al.* (2002) suggest that variations in the thickness of lava and dyke units along the Hess Deep, adjacent to the fast-spreading EPR, reflect temporal fluctuations in magma supply, while Stewart *et al.* (2002) analysed samples collected along a ∼25 km (370 000 yr) transect through the same area and showed that the high variability in magma composition observed over short distances and time periods results from multiple injections of melt into the crust rather than having an origin in a single, well-mixed magma reservoir.

(5) Wright *et al.*'s (2002) sidescan sonar study at 17°15′S on the EPR shows a good correlation between along-axis variation in fissure density and the relative age of lava flows, and with older lavas associated with increased fissure density. They also conclude that the structure of fast-spreading ridges is related to episodic cycles of magmatic and tectonic processes within second- to fourth-order segments, with dyke propagation along-axis a significant factor.

(6) White *et al.*'s (2002) observations of lava flow morphology and tectonic features at 9°–10°N on the EPR indicate that each third-order segment behaves as a single volcanic system with higher effusion rates near segment centres.

(7) Hilton *et al.* (1993) analysed lavas dredged from the Central Valu Fa Ridge in the Lau Basin and showed that their along-axis compositional and geochemical variations imply that this ridge segment is supplied by a number of separate magmatic systems. Collier & Sinha (1992) showed that the same ridge segment can be divided into three fourth-order segments based upon their bathymetric, morphological and magmatic characteristics, whose differences they attribute to cyclic magma supply and tectonic extension on the fourth-order segment length-scale and that each segment is at a

different phase in this cycle. Turner *et al.* (1999) and Day *et al.* (2001) showed that this pattern of segmentation and laterally variable melt supply is also mirrored in the along-axis velocity structure of layer 3, and Peirce *et al.* (2001) the along-axis gravity field.

Cyclic accretion therefore operates at all spreading rates, with the time frame of magma supply to the crust, the along-axis redistribution of melt and tectonic extension being the most likely cause of the observed morphological differences.

However, most work to date has focused mainly on seabed morphological and geochemical observations of segments of all scales, which provide only a limited insight into the formation of the oceanic crust and on the temporal and spatial variation in accretionary processes. By combining multibeam bathymetry, TOBI images, gravity and magnetic data with existing seismic velocity and CSEM-derived resistivity models of the whole crust and uppermost mantle together with an MT-derived resistivity model for the mantle to 100 km bsl, this study provides geophysical evidence for the relationships between tectono-magmatic cycles, subseafloor structure and the mode of segment construction along-axis. The cyclicity and along-axis variability of features in this model also explain the lack of observation of active crustal magmatic systems at slower-spreading rates as their observation is dependent on being in the right place at the right time within a cycle. The main results of this study are described below in the context of a unifying model of crustal accretion along an ∼100 km section of the Reykjanes Ridge (Fig. 19).

## THE MODEL

For most of the life cycle of a segment, far-field tectonic stresses generate brittle deformation of the crust at the ridge axis. Magma delivery takes place along the ridge trend in an episodic fashion that controls the initiation of an AVR tectono-magmatic cycle. As melt reaches the crust, the first AVR within a segment starts to form at the centre of upwelling orientated in the minimum stress direction, orthogonal to spreading.

As also observed during the Krafla eruptions onshore in Iceland, eruption commences with fissure volcanism (the *young* stage) and progresses to point-source volcanism, with the creation of conical and eventually flat-topped volcanoes (*adolescent* and *mature* stages, respectively). At Krafla, this progression in eruption style has been observed to take place within the same eruption cycle and over a very short period of time.

As the magmatic part of the cycle wanes, tectonic forces begin to dismember this AVR (*mature* stage) and brittle failure propagates north and south, facilitating the creation of subsequent AVRs in a pattern of progressively younger and shorter AVRs moving away from the original eruption location. The discontinuous nature of and periodicity in melt supply along-axis, therefore, limits the length to which the segment can evolve. However, as AVRs grow obliquely to the ridge axis their extent off-axis (i.e. their length) will also be controlled by the strength of the ageing lithosphere into which they propagate (Searle *et al.* 1998).

The repeated tectonic and magmatic phases continually build and destroy AVRs, with older AVRs generally being longer than younger ones and located at or near the focus of primary melt influx. The younger AVRs mark the location of most recent melt accumulation within the crust and hence the location of most recent magmatic activity. Each melt accumulation is sufficient to support of the order of ∼20 000 yr of accretion—corresponding to only ∼200 m of seafloor spreading on each flank at 10 mm $yr^{-1}$ half-rate. It is likely that older AVRs from earlier cycles are dismembered and rafted off-axis over the course of several cycles before they leave the neovolcanic zone.

Successive accretionary cycles are initiated by repeated influx of melt to the crust. Melt accumulated in the uppermost ∼50 km of the mantle is transported on a very short geological timescale to the crust where it accumulates at the segment centre and is then transported laterally, primarily through faults and fissures.

The episodic nature of melt delivery to the crust results in AVRs having a range of crustal structures and characteristics that are reflected not only in the seabed morphology but also in along-ridge-axis variations in AVR age and length, RMBA amplitude, magnetization intensity and local spreading-rate. When collectively analysed these features reveal that, in this study area on the Reykjanes Ridge, the second-order segment immediately north of the RAMESSES AVR comprises a set of five third-order AVR segments with an along-axis length of ∼70 km, typical of second-order segments elsewhere on the MAR. Tectono-magmatic accretion cycles operate both on the longer wavelength scale over the second-order segment as a whole, and on the smaller scale of individual AVRs. Within this second-order segment, AVR 4 appears to be the oldest and the longest of the five AVRs at 35 km; it has a locally thickened crust beneath its centre, and a low average magnetization and local spreading rate. AVR age and length decrease gradually to the south towards the 57°55′N second-order offset (Searle *et al.* 1994a) and north to another offset near 58°15′N.

The five AVRs studied, including one each from adjacent second-order segments, all have relative RMBA lows associated with their centres which reflect either an increase in crustal thickness of between 200 and 800 m and/or the presence of low-density zones, the latter corresponding to the presence of partial melt in the mid-lower crust. Larger mid-lower crustal density anomalies correspond to *young* AVRs undergoing magmatic construction while the increased crustal thicknesses correspond to *mature* AVRs at the end of their construction phase. The correlation between relative AVR age and length results from older AVRs having simply received more injections of melt and having, therefore, been able to extend further.

*Mature* AVRs are associated with relative magnetization intensity lows, while *young* AVRs show magnetization highs. The *young* AVRs located at the segment ends, therefore, have an extrusive layer that comprises fresher and more recently erupted basalt, or an axial magmatic system that contains magma that either has had time to fractionate before eruption or was already fractionated when it accumulated and erupted.

Spreading rate variations between individual AVRs indicate that the magmatic phase of the cycle locally 'speeds up' spreading by up to 20 per cent compared to older AVRs in their tectonic phase. This increase in spreading rate occurs for no more than ∼1–1.5 M yr (the finest timing resolution we can achieve in this study from magnetic reversals), after which spreading returns to that of the 'far-field' spreading rate for the ridge as a whole. AVR construction is also accompanied by asymmetric spreading in a pattern mirrored in the short-wavelength RMBA, where thinner crust is correlated with the direction of fastest spreading, either through differential tectonic extension or asymmetric magma injection into the crust.

Further support for our preferred model comes in the form of the observed asymmetry and cross-sectional form of the median valley south of 59°N. Thatcher & Hill (1995) propose that the dominant factors which influence the morphological expression of mid-ocean ridges are magmatism and tectonism, with magmatism being the dominant process accommodating plate separation and tectonism being the dominant process in producing seabed relief. They also conclude that variation in the rate of magmatism

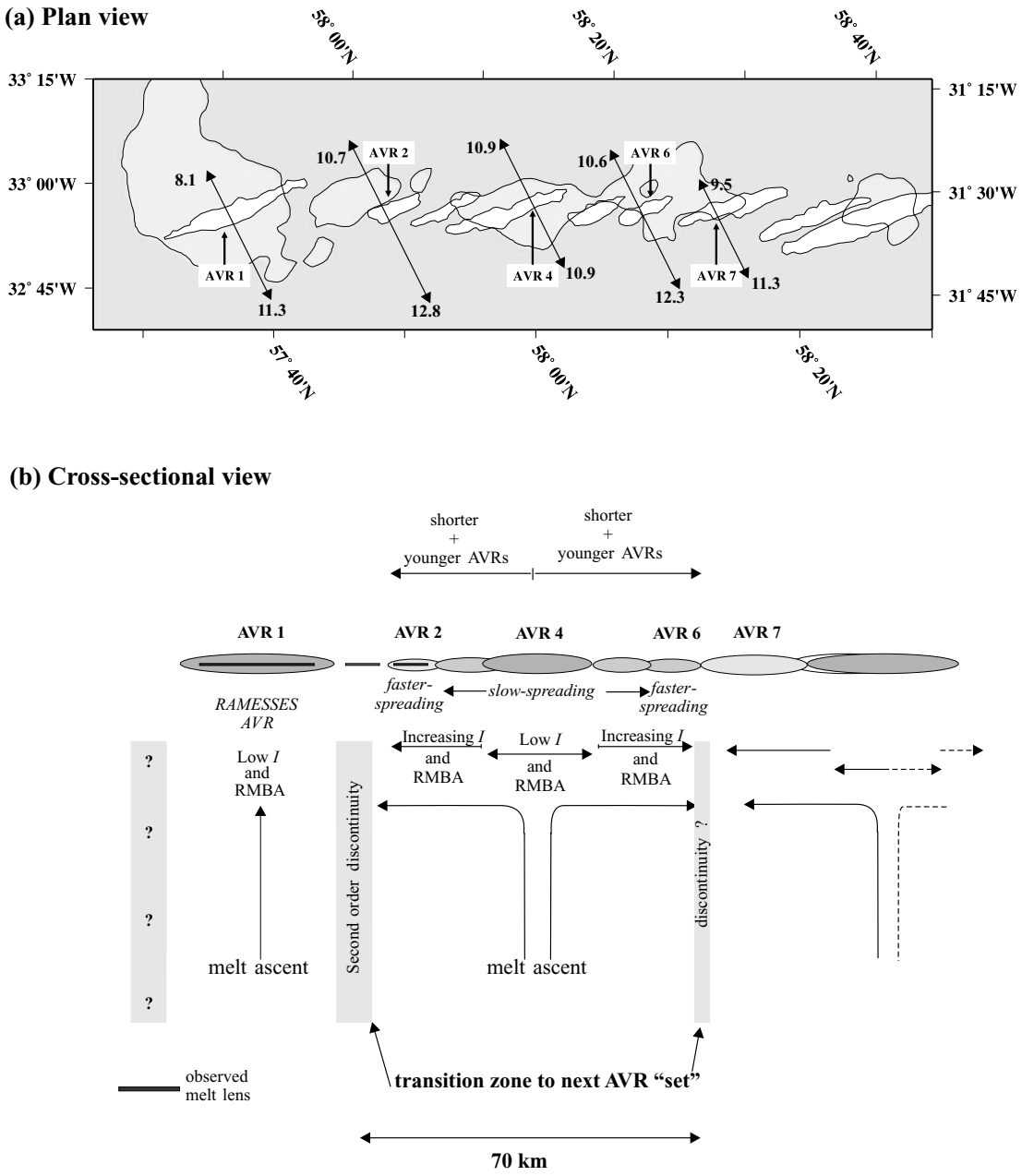


**Figure 19.** Model of segmentation and cyclicity of crustal accretion. (a) Schematic view of AVR location (white) superimposed on RMBA lows (light grey). Local half-spreading rates for the last 1.42 Ma are annotated in mm $yr^{-1}$. Note the correlation between asymmetric spreading and the asymmetric RMBA pattern. (b) Hypothesized pattern of mantle upwelling with a ~70 km wavelength, which explains the observed variations in AVR length, AVR age, RMBA magnitude, magnetization intensity (I) and spreading rate. A second-order segment is interpreted to comprise ~5 AVRs at this location. The locations of melt lenses imaged in the RAMESSES seismic data sets are shown for reference.

modulates the rate of normal faulting, which in turn influences the character of the rift topography. In Thatcher & Hill's (1995) model for the case of symmetrical spreading, throughout periods of increased magmatic accretion the rift valley floor will increase in width and normal faulting will be subdued, while during periods of decreased magmatic accretion tectonism and rift valley wall construction will dominate, with both feature types being preserved in the seabed morphology as it spreads away from the ridge axis. Thus if faulting and magmatism are continuous the model predicts that not only should the seabed morphology be symmetrical about the ridge axis, but that there should be no hiatus between fault terraces or significant changes in relief between those terraces. They also show that in the case of asymmetric spreading, the resulting seabed relief is more rugged on the more slowly accreting side.

Fig. 7 shows the off-axis seabed topography in the region of the RAMESSES AVR and the corresponding fault geometries. It also shows that the main fault terraces are separated by relatively unfaulted regions and that the seabed topography is asymmetric about the ridge axis. In addition, Topping (2002) and Peirce *et al.* (2005), interpreting a grid of multichannel seismic reflection profiles acquired across the RAMESSES AVR, show that there is a distinct asymmetry in the faulting pattern with terraces separated at 2–5 km (200 000–500 000 yr) intervals which also correspond to periods of enhanced magmatism as evidenced by a correspondingly thicker

extrusive layer within the upper crust. These observations, in the context of Thatcher & Hill's (1995) study, lend further support to cyclic rather continuous accretion and tectonism.

Although our model satisfies the observations and modelling of all data sets considered in this study, it is unlikely to be the only possible model. For example, it may be that faulting and magmatism are closely linked, taking place at the same time and throughout the life cycle of each AVR. In this alternative model, the atectonic (or the *magmatic*) phase of a tectono-magmatic cycle could simply be a manifestation of the on-going faulting being overprinted, or concealed, by frequent lava eruptions. However, the latter implies an effectively continuous magma supply which contradicts all of the evidence from the RAMESSES and other studies that crustal magma bodies at slow spreading rates are ephemeral and relatively short lived.

It is likely that our model could be improved and refined by the addition of more, and higher resolution, survey data. This should ideally include the collection, analysis and reliable dating of a dense array of fresh seabed samples; comprehensive photographic imaging; and a complete analysis of strain and spreading rates on both sides of the axis, on at least the length-scale (along and across axis) of an AVR. Such a comprehensive data set does not exist for any part of the mid-ocean ridge system—indeed the section of Reykjanes Ridge presented here is already amongst the most comprehensively studied parts of that system. In the context of all the available data from the Reykjanes Ridge, and the knowledge gleaned from studies of ridges at all spreading rates and settings, we believe that the model presented here provides the most consistent possible interpretation of the relationships between magmatic and tectonic processes, their cyclic variability and along-axis segmentation.

## 9 CONCLUSIONS

The results from this study provide convincing geophysical evidence for the episodic accumulation in and transport of melt from the mantle to the crust, which initiates and drives cycles of tectonic and magmatic phases of accretion. The conclusions, summarized below, primarily reflect processes operating at the AVR and larger scale, although they do also have implications for smaller-scale compositional variation. The conclusions are presented in scale order and the underlying assumptions upon which they are based can be found in the stated sections.

(1) The southern limit of any major hotspot influence on crustal thickness and magma production rates along the Reykjanes Ridge is ∼59°N. [Section 5.1]

(2) The shoaling seabed towards Iceland is mirrored in the FAA, which suggests that the elevated topographic swell associated with the Iceland hotspot is not in complete isostatic equilibrium, but is instead partly supported dynamically by processes associated with the mantle plume. Modelling shows that the swell is also partly compensated by a decrease in mantle density and a corresponding increase in crustal thickness heading towards the hotspot centre. [Section 5.1]

(3) A second-order segment is shown to be ∼70 km in length along-axis and comprises multiple third-order AVRs. A tectono-magmatic cycle operates over the entire segment length as well as at individual AVRs. [Section 7.1]

(4) AVRs undergo a life cycle from the *young* to *adolescent* stages of a magmatic phase when crustal construction occurs, through to the *mature* and *old* stages of a tectonic phase when AVRs are dismembered and rafted off-axis. However, at the very end of the magmatic phase AVRs may be rejuvenated by late stage volcanism. [Section 4; Section 7.1]

(5) Volcanism starts first at the AVR at the segment centre then propagates outwards along the segment to build other AVRs as the cycle progresses. [Section 6.8; Section 8]

(6) AVRs are typically older and longer at the segment centre and younger and shorter at segment ends. Older AVRs generally have lower average magnetization intensities than younger AVRs, suggesting that basalts there have been extruded for longer and have undergone more low-temperature oxidation or that the erupted lavas were less fractionated. [Section 4; Section 7]

(7) Gravity models of individual AVRs support a segment-scale model where cyclic injections of melt gradually build adjacent AVRs. Density anomalies beneath *young* AVRs are consistent with the presence of partial melt in the mid-lower crust, indicating that they are presently undergoing magmatic construction, while slightly older AVRs, from *young* to *adolescent* in age, have smaller density anomalies consistent with slightly less melt in the crust and with declining magmatic accretion. *Mature* AVRs have thicker crust beneath their centres, suggesting that they are at the very end of the magmatic phase of their cycle, with the crust built to its maximum thickness by repeated injections of melt. [Section 4; Section 6]

(8) An ∼20 per cent increase in spreading rate associated with young AVRs detectable over the last 1–1.5 Ma suggests that magmatic accretion increases the local spreading rate. Asymmetry in spreading rate results in thinner crust underlying the faster spreading ridge flank. [Section 7.2]

The above conclusions support a model of crustal accretion along ∼100 km of the Reykjanes Ridge that explains tectono-magmatic cycles in terms of patterns of mantle upwelling and segmentation along the ridge axis. Far-field tectonic stresses result in spreading-orthogonal brittle deformation of the crust in the neovolcanic zone, with fractures tapping initially the upwelling melt. An AVR is constructed over these fractures, initially through fissure volcanism (the *young* stage), and progressively point-source volcanism dominates, with the creation of conical and eventually flat-topped volcanoes (*adolescent* and *mature* stages respectively). Brittle failure propagates away from the initial point of magma injection in both directions along-axis. These new fractures laterally tap the melt supply, resulting in the creation of new AVRs and the pattern of progressively younger and shorter AVRs towards the segment ends. As the magmatic part of the cycle wanes, tectonic forces dismember AVRs (the *old* stage). This cycle repeats along the ridge axis and through time, initiated by the episodic influx of melt from the uppermost ∼50 km of the mantle below.

Finally, the results of this study are compatible with all other geophysical experiments undertaken south of ∼59°N on the Reykjanes Ridge and all crustal thickness determinations along its entire length. It represents a fully integrated geophysical study of the relationship between the temporal variations in crustal accretionary processes at slow-spreading ridges and their along-axis segmentation. It has revealed that tectono-magmatic cycles of accretion do operate both at the third-order AVR-scale and also over the entire second-order segment which the AVRs studied here comprise.

## ACKNOWLEDGMENTS

This research was supported by the University of Durham via a PhD studentship (AG). Figures were created using the Generic Mapping Tools of Wessel & Smith (1995). Further information and larger versions of Figs 5 & 8 can be found on the RAMESSES www

home page (http://www.dur.ac.uk/ramesses/) or by e-mailing the authors. We thank the anonymous reviewers for their constructive and detailed comments and Roger Searle for access to the TOBI data.

## REFERENCES


Applegate, B. & Shor, A.N., 1994. The northern Mid-Atlantic and Reykjanes Ridges: Spreading centre morphology between 55°50′N and 63°00′N, *J. geophys. Res.,* **99,** 17935–17 956.

Bazin, S. *et al.*, 2001. Three-dimensional shallow crustal emplacement at the 9°03′N overlapping spreading centre on the East Pacific Rise: correlations between magnetization and tomographic images, *J. geophys. Res.,* **106,** 16 101–16 117.

Bunch, A.W.H. & Kennett, B.L.N., 1980. The crustal structure of the Reykjanes Ridge at 59°30′N, *Geophys. J. R. astr. Soc.,* **61,** 141–166.

Cande, S.C. & Kent, D.V., 1995. Revised calibration of the geomagnetic polarity timescale for the Late Cretaceous and Cenozoic, *J. geophys. Res.,* **100,** 6093–6095.

Carbotte, S. & Macdonald, K., 1992. East Pacific Rise 8°−10°30′N: evolution of ridge segments and discontinuities from SeaMARC II and three-dimensional magnetic studies, *J. geophys. Res.,* **97,** 6959–6982.

Carlson, R.L. & Raskin, G.S., 1984. Density of the oceanic crust, *Nature,* **311,** 555–558.

Collier, J.S. & Sinha, M.C., 1992. Seismic mapping of a magma chamber beneath the Valu Fa Ridge, Lau Basin, *J. geophys. Res.,* **97,** 14 031–14 053.

Cormier, M.-H., Macdonald, K.C. & Wilson, D.S., 1995. A three-dimensional gravity analysis of the East Pacific Rise from 18° to 21°30′S, *J. geophys. Res.,* **100,** 8063–8082.

Day, A.J., Peirce, C. & Sinha, M.C., 2001. Three-dimensional crustal structure and magma chamber geometry at the intermediate-spreading, back-arc Valu Fa Ridge, Lau Basin—results of a wide-angle seismic tomographic inversion, *Geophys. J. Int.,* **146,** 31–52.

DeMets, C., Gordon, R.G., Argus, D.F. & Stein, S., 1990. Current plate motions, *Geophys. J. Int.,* **101,** 425–478.

Detrick, R.S., Needham, H.D. & Renard, V., 1995. Gravity anomalies and crustal thickness variations along the Mid-Atlantic Ridge between 33°N and 40°N, *J. geophys. Res.,* **100,** 3767–3787.

Fleischer, U., 1974. The Reykjanes Ridge: A summary of geophysical data, in *Geodynamics of Iceland and the North Atlantic Area,* pp. 17–31, ed. Kristjansson, D., Reidel, Norwell, Massachusetts.

Forsyth, D.W. & Wilson, B., 1984. Three dimensional temperature structure of a ridge-transform-ridge system, *Earth planet. Sci. Lett.,* **70,** 355–362.

Fujiwara, T., Lin, J., Matsumoto, T., Kelemen, P.B., Tucholke, B.E. & Casey, J.F., 2003. Crustal evolution of the Mid-Atlantic Ridge near the Fifteen-Twenty Fracture Zone in the last 5 Ma, *Geochem. Geophys. Geosyst.,* **4**(3), 1–25.

Gardiner, A.B., 2003. Segmentation and cycles of crustal accretion at mid-ocean ridges: a study of the Reykjanes Ridge, *PhD thesis,* University of Durham (unpublished), p. 177.

Gee, J. & Kent, D., 1994. Variation in layer 2A thickness and the origin of the central anomaly magnetic high, *Geophys. Res. Letts.,* **21,** 297–300.

German, C.R. *et al.*, 1994. Hydrothermal activity on the Reykjanes Ridge: the Steinahóll vent field at 63°06′N, *Earth planet. Sci. Lett.,* **121,** 647–654.

Heinson, G.S., Constable, S.C. & White, A., 2000. Episodic melt transport at a mid-ocean ridge inferred from magnetotelluric sounding, *Geophys. Res. Letts.,* **27,** 2317–2320.

Hilton, D.R., Hammerschmidt, K., Loock, G. & Friedrichsen, H., 1993. Helium and argon isotope systematics of the Lau Basin and Valu Fa Ridge: evidence of crust/mantle interactions in a back-arc basin, *Geochim. cosmochim. Acta,* **57,** 2819–2841.

Hooft, E.E. & Detrick, R.S., 1993. The role of density in the accumulation of basaltic melt at mid-ocean ridges, *Geophys. Res. Letts.,* **20,** 423–426.

Hooft, E.E., Schouten, H. & Detrick, R.S., 1996. Constraining crustal emplacement processes from the variation in seismic layer 2A thickness at the East Pacific Rise, *Earth planet. Sci. Lett.,* **142,** 289–309.

Ito, G., 2001. Reykjanes 'V'-shaped ridges originating from a pulsing and dehydrating mantle plume, *Nature,* **411,** 681–684.

Johnson, H.P. & Atwater, T., 1977. Magnetic study of basalts from the MAR, lat. 37°N, *Geol. soc. Am. Bull.,* **88,** 637–647.

Johnson, H.P. & Hall, J.M., 1978. A detailed rock magnetic and opaque mineralogy study of basalts from the Nazca plate, *Geophys. J. R. astr. Soc.,* **52,** 45–64.

Johnson, H.P., Patten, D.V. & Sager, W.S., 1996. Age-dependent variation in the magnetization of seamounts, *J. geophys. Res.,* **101,** 13 701–13 714.

Jones, S.M., White, N. & Maclennan, J., 2002. V-shaped ridges around Iceland: implications for spatial and temporal patterns of mantle convection, *Geochem. Geophys. Geosyst.,* **3**(10), 1–23.

Karson, J.A., Tivey, M.A. & Delaney, J.R., 2002. Internal structure of uppermost oceanic crust along the Western Blanco Transform Scarp: implications for subaxial accretion and deformation at the Juan de Fuca Ridge, *J. geophys. Res.,* **107,** EPM 1-1–1-24.

Keeton, J.A., Searle, R.C., Parsons, B., White, R.S., Murton, B.J., Parson, L.M., Peirce, C. & Sinha, M.C., 1997. Bathymetry of the Reykjanes Ridge, *Marine geophys. Res.,* **19,** 55–64.

Kuo, B.-Y. & Forsyth, D.W., 1988. Gravity anomalies of the ridge-transform system in the south Atlantic between 31° and 34.5°S upwelling centres and variations in crustal thickness, *Marine geophys. Res.,* **10,** 205–232.

Lawson, K., Searle, R.C., Pearce, J.A., Browning, P. & Kempton, P., 1996. Detailed volcanic geology of the MARNOK area, Mid-Atlantic Ridge north of Kane transform, in *Tectonic, magmatic, hydrothermal and biological segmentation of mid-ocean ridges,* Vol. 118, pp. 61–102, eds. MacLeod, C.J., Tyler, P.A. & Walker, C.L., Geol. Soc. Spec. Pub.

Lee, S.-M. & Searle, R.C., 2000. Crustal magnetization of the Reykjanes Ridge and implications for its along-axis variability and the formation of axial volcanic ridges, *J. geophys. Res.,* **105,** 5907–5930.

Lin, J. & Phipps Morgan, J., 1992. The spreading rate dependence of three-dimensional mid-ocean ridge gravity structure, *Geophys. Res. Letts.,* **19,** 13–16.

Lin, J., Purdy, G.M., Schouten, H., Sempere, J.C. & Zervas, C., 1990. Evidence from gravity data for focused magmatic accretion along the Mid-Atlantic Ridge, *Nature,* **344,** 627–632.

Lowrie, W., 1977. Intensity and direction of magnetization in oceanic basalts, *J. geol. Soc. Lon.,* **133,** 61–82.

Macdonald, K.C., 1977. Near-bottom magnetic anomalies, asymmetric spreading, oblique spreading and tectonics of the Mid-Atlantic Ridge near 37°N, *Geol. soc. Am. Bull.,* **88,** 541–555.

Macdonald, K.C., Miller, S.P., Huestis, S.P. & Spiess, F.N., 1980. Three-dimensional modelling of a magnetic reversal boundary from inversion of deep-tow measurements, *J. geophys. Res.,* **85,** 3670–3680.

MacGregor, L.M., Constable, S. & Sinha, M.C., 1998. The RAMESSES experiment III: controlled source electromagnetic sounding of the Reykjanes Ridge at 57°45′N, *Geophys. J. Int.,* **135,** 772–789.

Magde, L.S., Detrick, R.S. & the, TERA group, 1995. Crustal and upper mantle contribution to the axial gravity anomaly at the southern East Pacific Rise. *J. geophys. Res.,* **100,** 3747–3766.

Nafe, J.E. & Drake, C.L., 1957. Variation with depth in shallow and deep water marine sediment of porosity, density and the velocities of compressional and shear waves, *Geophysics,* **22,** 523–553.

Nafe, J.E. & Drake, C.L., 1962. Physical properties of marine sediments. in *The Sea,* Vol. 3, pp. 794–815, ed. Hill, M.N., Wiley, New York.

Navin, D.A., Peirce, C. & Sinha, M.C., 1998. The RAMESSES experiment—II. Evidence for accumulated melt beneath slow-spreading ridge from wide-angle refraction and multichannel reflection seismic profiles, *Geophys. J. Int.,* **135,** 746–772.

Owens, R.B., 1991. An investigation of marine anomalies from Reykjanes Ridge 58°N 32°20′W, *MSc thesis,* University of Durham (unpublished), p. 54.

Parker, R.L. & Huestis, S.P., 1974. The inversion of magnetic anomalies in the presence of topography, *J. geophys. Res.,* **79,** 1587–1593.

Parson L.M., 1993. Sidescan sonar and swath bathymetry investigation of the Reykjanes Ridge, southwest of Iceland, R/V Maurice Ewing EW9008 Cruise Report (unpublished), p. 8.

Parson, L.M. *et al.*, 1993. En echelon axial volcanic ridges at the Reykjanes Ridge: a life cycle of volcanism and tectonics, *Earth planet. Sci. Lett.,* **117,** 73–87.

Pedley, R.C., Busby, J.P. & Dabek, Z.K., 1993. GRAVMAG User Manual—Interactive 2.5D gravity and magnetic modelling, *British Geological Survey, Technical Report WK/93/26/R,* p. 73.

Peirce, C. & Navin, D.A., 2002. The RAMESSES experiment-V. Crustal accretion at axial volcanic ridge segments-a gravity study at 57°45′N on the slow-spreading Reykjanes Ridge, *Geophys. J. Int.,* **149,** 76–94.

Peirce, C. & Sinha, M.C., 1998. RAMESSES II—Reykjanes Ridge axial melt experiment: structural synthesis from electromagnetics and seismic, RRS Discovery 235c Cruise Report (unpublished), p. 38.

Peirce, C., Turner, I.M. & Sinha, M.C., 2001. Crustal structure, accretionary processes and rift propagation: a gravity study of the intermediate-spreading Valu Fa Ridge, *Geophys. J. Int.,* **146,** 53–173.

Peirce, C., Sinha, M.C., Topping, S. & Gill, C., 2005. Morphology and genesis of slow-spreading ridges—seabed scattering and seismic imaging within the oceanic crust, *Geophys. J. Int.,* in prep.

Phipps Morgan, J. & Forsyth, D.W., 1988. Three-dimensional flow and temperature perturbations due to a transform offset: effects on oceanic crustal and mantle structure, *J. geophys. Res.,* **93**(B4), 2955–2966.

Prince, R.A. & Forsyth, D.W., 1988. Horizontal extent of anomalously thin crust near the Vema fracture zone from the 3-D analysis of gravity anomalies, *J. geophys. Res.,* **93,** 8051–8063.

Rouse, I.P., 1991. TOBI: a deep-towed sonar system, in colloquium on 'Civil applications of sonar systems', *Institute of Electrical Engineers*, Digest no. 1991/028, 7/1–7/5.

Sandwell, D.T. & Smith, W.H.F., 1997. Marine gravity anomaly from Geosat and ERS-1 satellite Altimetry, *J. geophys. Res.,* **102,** 10 039–10 054.

Sauter, D., Parson, L., Mendel, V., Rommevaux-Jestin, C., Gomez, O., Briais, A., Mevel, C., Tamaki, K. & the FUJI scientific team, 2002. TOBI sidescan sonar imagery of the very slow-spreading Southwest Indian Ridge: evidence for along-axis magma distribution, *Earth planet. Sci. Lett.,* **199,** 81–95.

Schouten, H., Tivey, M.A., Fornari, D.J. & Cochran J.R., 1999. Central anomaly magnetization high: constraints on the volcanic construction and architecture of seismic layer 2A at a fast-spreading mid-ocean ridge, the EPR at 9°30′–50′N, *Earth planet. Sci. Lett.,* **169,** 37–50.

Searle, R.C., Field, P.R. & Owens, R.B., 1994a. Segmentation and a non-transform ridge offset on the Reykjanes Ridge near 58°N, *J. geophys. Res.,* **99,** 24 159–24 172.

Searle, R.C., Parsons, B.E. & White, R.S., 1994b. Multibeam bathymetric and potential field studies of the Reykjanes Ridge, RRS Charles Darwin 87 Cruise Report (unpublished), p. 43.

Searle, R.C., Keeton, J.A., Owens, R.B., White, R.S., Mecklenburgh, R., Parsons, B. & Lee, S.-M., 1998. The Reykjanes Ridge: Structure and tectonics of a hotspot influenced, slow-spreading ridge, from multibeam bathymetry, gravity and magnetic investigations, *Earth planet. Sci. Lett.,* **160,** 463–478.

Sinha, M.C., Peirce, C. & Constable, S., 1994. An integrated geophysical investigation of the axial volcanic region of the Reykjanes Ridge at 57°45′N, RRS Charles Darwin 81 Cruise report (unpublished), p. 39.

Sinha, M.C., Navin, D.A., MacGregor, L.M., Constable, S., Peirce, C., White, A., Heinson, G. & Inglis, M.A., 1997. Evidence for accumulated melt beneath the slow-spreading Mid-Atlantic Ridge, *Phil. Trans. R. Soc. Lond.,* A, **355,** 233–253.

Sinha, M.C., Constable, S., Peirce, C., White, A., Heinson, G., MacGregor, L.M. & Navin, D.A., 1998. Magmatic processes at slow-spreading ridges: implications of the RAMESSES experiment, Mid-Atlantic Ridge at 57°N, *Geophys. J. Int.,* **135,** 731–745.

Smallwood, J.R., White, R.S. & Minshull, T.A., 1995. Sea-floor spreading in the presence of the Iceland plume—the structure of the Reykjanes Ridge at 61°40′N, *J. geol. Soc. Lond.,* **152,** 1023–1029.

Sohn, R.A., Webb, S.C., Hildebrand, J.A. & Cornuelle, B.D., 1997. Three-dimensional tomographic velocity structure of the upper crust, CoAxial segment, Juan de Fuca Ridge: implications for on-axis evolution and hydrothermal circulation, *J. geophys. Res.,* **102,** 17 679–17 695.

Sparks, D.W., Parmentier, E.M. & Phipps Morgan, J., 1993. Three-dimensional mantle convection beneath a segmented spreading centre: implications for along-axis variations in crustal thickness and gravity, *J. geophys. Res.,* **98,** 21 977–21 995.

Stewart, M.A, Klein, E.M. & Karson, J.A., 2002. Geochemistry of dikes and lavas from the north wall of the Hess Deep Rift: insights into the four-dimensional character of crustal construction at fast-spreading mid-ocean ridges, *J. geophys. Res.,* **107,** EPM 4-1–4-23.

Talwani, M., Windsich, C.C. & Langseth, M.G., 1971. Reykjanes Ridge Crest: a detailed geophysical study, *J. geophys. Res.,* **76,** 473–517.

Thatcher, W. & Hill, D.P., 1995. A simple model for the fault-generated morphology of slow-spreading mid-ocean ridges, *J. geophys. Res.,* **100,** 561–570.

Tolstoy, M., Harding, A.J. & Orcutt, J.A., 1993. Crustal thickness on the Mid-Atlantic Ridge: Bull's-eye gravity anomalies and focused accretion, *Science,* **263,** 726–729.

Topping, S., 2002. RAMESSES II: seismic reflections at the Mid-Atlantic ridge from analysis of real and synthetic data, *PhD thesis,* University of Cambridge (unpublished), pp. 196.

Turner, I.M., Peirce, C. & Sinha, M.C., 1999. Seismic imaging of the axial region of the Valu Fa Ridge, Lau Basin—the accretionary processes of an intermediate back-arc spreading ridge, *Geophys. J. Int.,* **138,** 495–519.

Vogt, P.R., 1971. Asthenospheric motion recorded by the ocean floor south of Iceland, *Earth planet. Sci. Lett.,* **13,** 153–160.

Weir, N.R.W., White, R.S., Brandsdottir, B., Einarsson, P., Shimamura, H., Shiobara, H. & the RISE Fieldwork Team, 2001. Crustal structure of the northern Reykjanes Ridge and Reykjanes Peninsula, southwest Iceland, *J. geophys. Res.,* **106,** 6347–6368.

Wessel, P. & Smith, W.H.F., 1995. New version of the Generic Mapping Tools released, *EOS, Trans. Am. geophys. Un.,* **76,** 329.

White, R.S., McKenzie, D. & O'Nions, R.K., 1992. Oceanic crustal thickness from seismic measurements and rare earth element inversions, *J. geophys. Res.,* **97,** 19 683–19 715.

White, S.M., Haymon, R.M., Fornari, D.J., Perfit, M.R. & Macdonald, K.C., 2002. Correlation between volcanic and tectonic segmentation of fast-spreading ridges: evidence from volcanic structures and lava flow morphology on the East Pacific Rise at 9°–10°N, *J. geophys. Res.,* **107,** EPM 7-1–7-20.

Wright, D.J., Haymon, R.M., White, S.M. & Macdonald, K.C., 2002. Crustal fissuring on the crest of the southern East Pacific Rise at 17°15′N-40′S, *J. geophys. Res.,* **107,** EPM 5-1–5-14.

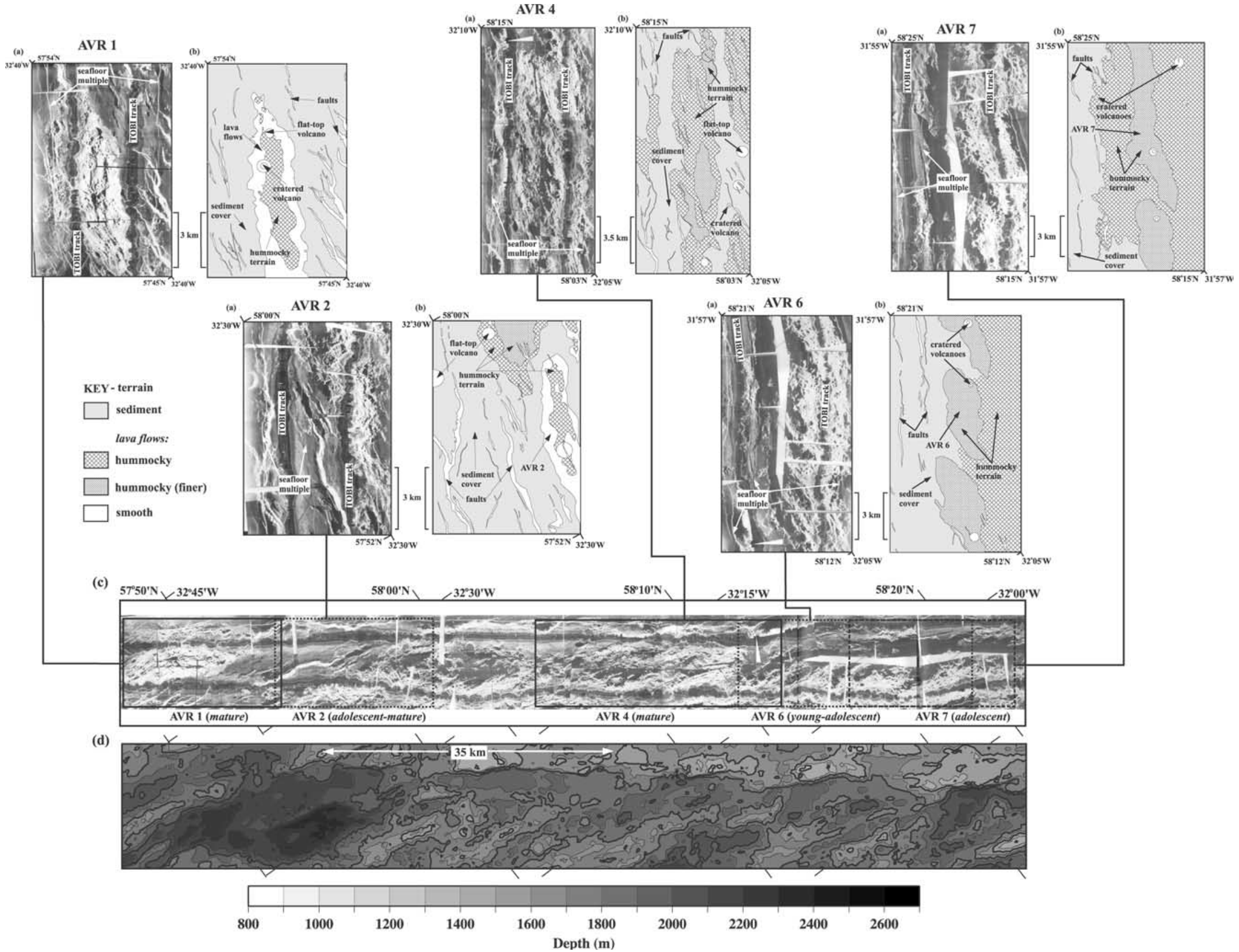


**Figure 5.** TOBI data interpretation for AVRs in area C. For each AVR, numbered according to its position along-axis: (a) TOBI data and (b) its detailed interpretation. Lines from the small TOBI data panels show the AVR locations and relative ages on (c) the main TOBI image. (d) Coincident multibeam bathymetry data to assist AVR interpretation in (b). Bathymetric contours are plotted at 100 m intervals. See Fig. 10 for AVR location along-axis.

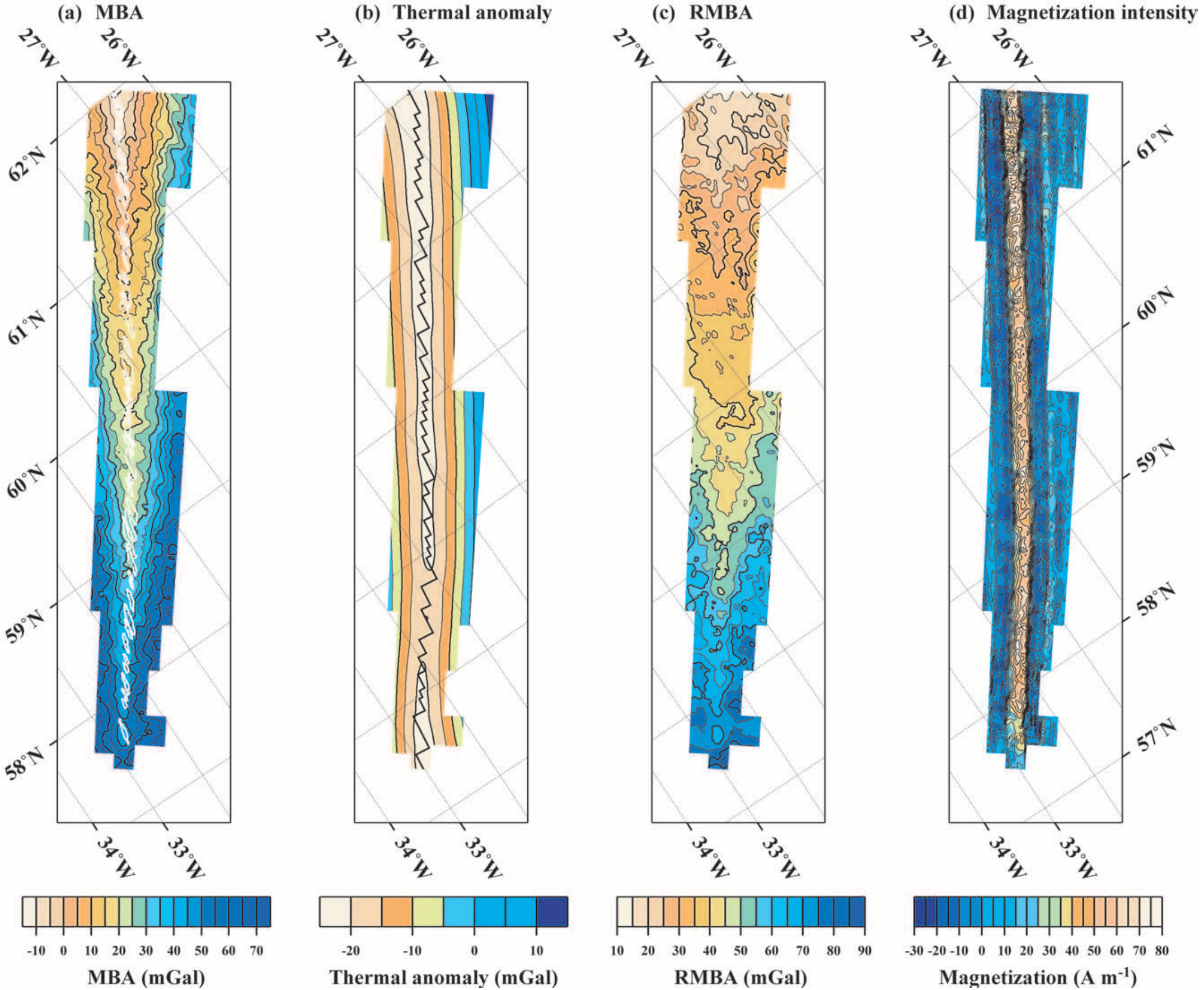


**Figure 8.** (a) MBA calculated by subtracting the gravitational effect of the simple crustal model shown in Fig. 7. The main features of the MBA are small relative lows associated with individual AVR segments and a general decrease in anomaly amplitude towards Iceland along the ridge axis. AVR footprints of Keeton *et al.* (1997) are superimposed in white. AVR 1 is the most southerly and AVR numbers increment northwards. (b) Thermal anomaly due to the gravitational effect of passive upwelling at the ridge axis, calculated by subdividing the ridge into a number of ridge-transform-ridge segments (solid line) as defined by the AVR locations shown in (a). The thermal anomaly follows the overall ridge trend with a low of −20 mGal at the ridge axis. (c) RMBA calculated by subtracting the thermal anomaly from the MBA. Features described for the MBA are still visible indicating that they are not thermal effects related to passive upwelling but represent deviations from the simple initial crustal model, either in terms of crustal density and/or thickness and/or mantle density anomalies. (d) Magnetization intensity solution obtained by inversion of the magnetic anomaly with topographic effects removed. Magnetization intensities follow the ridge trend. A central anomaly magnetic high is visible and follows the ridge axis. On a short-wavelength scale, this is discontinuous with local highs associated with individual AVRs. Contours are plotted at 5 mGal intervals in (a)–(c) and at 10 A $m^{-1}$ intervals in (d).